Understanding Membranes and Vesicles: A Personal Recollection of the Last Two Decades

Reinhard Lipowsky

Denken ohne Erfahrung ist leer, Erfahrung ohne Denken ist blind.
(*Thought without experience is empty, experience without thought is blind.*)

Immanuel Kant

Abstract Biomembranes consist of fluid bilayers built up from many lipid and protein components. The membrane fluidity has two important consequences. First, the molecular components can undergo fast lateral transport within the membranes, a necessary prerequisite for the formation and remodelling of intramembrane compartments. Second, the fluidity leads to unusual elastic properties of the membranes that allow them to "escape into the third dimension." Intramembrane compartments can be formed by lipid phase separation, now observed for many ternary lipid mixtures, or by heterogeneous environments that lead to an ambience-induced segmentation of the membranes. Because of their unusual elastic properties, the membranes can attain many different shapes and undergo striking shape transformations, which reflect their ability to respond locally to external perturbations by changes in their curvature. Several molecular mechanisms for local curvature generation have been identified including membrane-anchored polymers, adsorption or depletion layers of solutes, and membrane-bound proteins. The local curvature generation is intimately related to the concept of a preferred or spontaneous curvature that describes the asymmetry between the two leaflets of the bilayer membrane. New methods to determine the spontaneous curvature in a reliable manner have been recently developed, based on spontaneous or force-induced tubulation of giant vesicles. The spontaneous curvature plays a pivotal role both for the engulfment of nanoparticles by membranes and for the wetting of membranes by aqueous droplets, two membrane processes that remain to be further elucidated.

R. Lipowsky (✉)
Theory & Bio-Systems, Max Planck Institute of Colloids and Interfaces, Potsdam, Germany
e-mail: lipowsky@mpikg.mpg.de

P. Bassereau, P. Sens (eds.), *Physics of Biological Membranes*,
https://doi.org/10.1007/978-3-030-00630-3_1

The spontaneous curvature also determines the exergonic or endergonic nature of membrane fusion and fission.

Keywords Biomembranes · Curvature · Tubulation · Nanoparticle engulfment · Membrane wetting

1 Introduction

Patricia Bassereau and Pierre Sens asked me to write an introductory chapter that provides a personal account of the "most interesting and surprising developments in membrane physics" during the last two decades, i.e., since the publication of the "green book" in 1995 [1]. The latter book on "Structure and Dynamics of Membranes" was edited by Erich Sackmann and myself, a longsome process that took several years. During the last decade, we discussed, once in a while, the possibility of a new edition but I never found the time to think seriously about such a venture. The present chapter gives me the opportunity to briefly review a few aspects of membranes and vesicles that I would definitely want to include in a putative new edition of the "green book."

The chapter is organized as follows. The following Sects. 2–5 address several aspects that caught my attention already in the 1990s and underwent important developments during the last 20 years: Fluid domains or rafts in fluid membranes; segmentation of membranes by heterogeneous environments; emergence of membrane curvature on nanoscopic scales; as well as local curvature generation and spontaneous curvature. At the end of Sect. 3, it is argued that intracellular heterogeneities close to the membranes act to suppress the separation and coexistence of lipid phases in vivo. In Sect. 5, membrane-bound proteins are viewed as Janus particles with strongly nonspherical shapes.

The subsequent Sects. 6–9 deal with four aspects that I found particularly interesting during the last couple of years: Two distinct mechanisms for the formation of membrane nanotubes as provided by spontaneous curvature and locally applied forces; the interplay between these two tubulation mechanisms; the engulfment of nanoparticles by membranes; and the wetting of membranes by aqueous two-phase systems. Section 7 describes the interplay of spontaneous and force-induced tubulation in a quantitative manner. Section 9 emphasizes that all lipid compositions and aqueous two-phase systems that have been studied so far undergo complete-to-partial wetting transitions and that the nucleation and growth of droplets at membranes depends strongly on the spontaneous curvature. Finally, Sect. 10 explains how this curvature affects the exergonic or endergonic nature of membrane fusion and fission, the most important topology-transforming membrane processes. At the end, I give a brief summary and a short outlook on open questions and future studies. In order to produce a readable piece, I had to focus on a few aspects of membranes and vesicles and, thus, had to omit other intriguing aspects, many of which will be covered in later chapters of this book.

The presentation is intuitive and largely nontechnical but, as a theoretical physicist, I cannot refrain from displaying some equations. Following the motto "As simple as possible but not simpler" of Albert Einstein, all displayed equations are short and provide simple relationships between a small number of parameters. In addition, all of these parameters can now be measured in experiments and/or simulations. One such parameter that plays a prominent role in the following is the spontaneous (or preferred) curvature which describes the local asymmetry between the two leaflets of bilayer membranes. A much more detailed account of the underlying theory will be given elsewhere [2].

2 Fluid Domains and Rafts in Fluid Membranes

Biological and biomimetic membranes are fluid, contain several molecular components, and represent two-dimensional systems. As a consequence, they should be able to undergo phase separation into two types of fluid domains, in close analogy to macroscopic liquid mixtures in three dimensions. This conclusion seems quite obvious from a theoretical point of view but, at the beginning of the 1990s, it was rather difficult to find experimental evidence for it. In fact, when I first submitted my theory on domain-induced budding [3, 4] to *Nature*, the editors finally rejected it after an extended review process because they thought that the underlying idea of fluid-fluid coexistence in bilayer membranes was "too speculative."

2.1 Intramembrane Domains in Ternary Lipid Mixtures

This situation has now changed completely because many ternary lipid mixtures have been identified which exhibit two coexisting fluid phases, a liquid-ordered and a liquid-disordered phase, see Fig. 1. These mixtures consist of a saturated lipid such as sphingomyelin, an unsaturated phospholipid, and cholesterol. The intense experimental study of these mixtures was triggered by the proposal [8] that biological membranes contain intramembrane domains or rafts that are rich in sphingomyelin and cholesterol. In order to directly visualize the different domains formed in lipid vesicles, it was also crucial to find appropriate fluorescent probes that have a preference for one of the two fluid phases [6, 9–11].

Direct evidence for the formation of two types of fluid domains was provided by single particle tracking that showed that both phases exhibit relatively fast lateral diffusion [10]. In addition, using giant unilamellar vesicles, several theoretical predictions [3, 5, 12, 13] could be directly confirmed: the growth and coalescence of small domains into larger ones [11]; the budding of the more flexible domains [6, 11]; and the shift of the domain boundary away from the neck of the bud [14, 15]. So far, this domain boundary shift provides the only method to estimate the difference between the Gaussian curvature moduli for the two types of membrane domains.

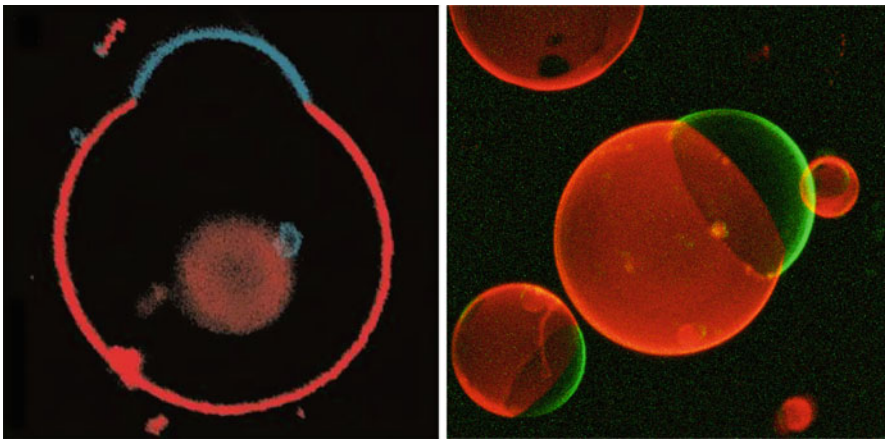

Fig. 1 Domain-induced budding of vesicles as theoretically predicted in [3, 5] and observed by fluorescence microscopy in [6, 7]: (left) cross section through a vesicle that formed two domains after a decrease in temperature [6]; and (right) three-dimensional confocal scan of a two-domain vesicle that was formed by electrofusion [7]. In both cases, the vesicle membrane is composed of DOPC, sphingomyelin, and cholesterol, doped with small concentrations of two fluorescent probes

Phase separation in ternary lipid mixtures has now been observed for a variety of membrane systems including giant vesicles [6, 10, 11, 15–17], solid-supported membranes [18–20], hole-spanning (or black lipid) membranes [21], as well as pore-spanning membranes [22]. The phase diagrams of such three-component membranes have been determined using spectroscopic methods [23] as well as fluorescence microscopy of giant vesicles and X-ray diffraction of membrane stacks [24–27]. Somewhat surprisingly, fluid–fluid coexistence has even been found in giant plasma membrane vesicles that contain a wide assortment of different lipids and proteins [28, 29].

2.2 Lipid Phase Domains or Rafts In Vivo

As far as biological membranes are concerned, the existence and size of sphingomyelin- and cholesterol-enriched rafts as proposed in [8] is still a matter of ongoing debate. It is generally accepted that the diameter of these rafts is below the diffraction limit of conventional optical microscopy, i.e., below 200 nm, see, e.g., [30]. However, even superresolution microscopy methods such as STED [31, 32] could not provide a reliable estimate but only an upper bound for the raft size: the STED measurements indicated that, for the plasma membranes of mammalian cells, the raft diameter does not exceed 20 nm [31]. The search for rafts in biological membranes as pursued with different experimental techniques has been critically reviewed in [33].

2.3 Intramembrane Domains Arising from Protein Clusters

In contrast to lipid phase domains, the formation of intramembrane domains via the clustering of membrane proteins is frequently observed in vivo. One example is provided by clathrin-dependent endocytosis which is used to internalize membrane-bound receptors as well as cargo such as receptor-bound ligands or nanoparticles. During this process, a strongly asymmetric membrane domain is formed with receptors or receptor–ligand complexes on its outer (exoplasmic) face and a thick protein coat consisting of adaptor proteins and clathrin triskelions on its inner (cytoplasmic) face. Therefore, clathrin-dependent endocytosis can be understood as a domain-induced budding process that is governed by the membrane's spontaneous curvature. When the endocytic vesicles contain nanoparticles or other types of cargo, the uptake of this cargo becomes maximal at a certain, optimal cargo size [34] as experimentally observed for the uptake of gold nanoparticles by HeLa cells [35, 36]. The mechanism of domain-induced budding should also be responsible for membrane budding arising from the clustering of Shiga toxin [37] and from the sequential adsorption of ESCRT proteins [38].

3 Segmentation of Membranes by Heterogeneous Environments

As we move along a biological membrane, we typically encounter changes in the molecular composition of the aqueous environment and, thus, changes in the local interactions between this environment and the membrane molecules. One interesting example is provided by the interactions between the plasma membrane of a eukaryotic cell and its cytoskeletal cortex. Because different membrane molecules differ in their affinity to the cytoskeletal proteins, the membrane is partitioned into different segments in which certain lipids and/or membrane proteins are enriched or depleted.

3.1 Lateral Diffusion in Cell Membranes

This ambience-induced segmentation of the plasma membrane can be revealed by studying the lateral diffusion of the membrane molecules using single particle tracking [39–42], see Fig. 2. This figure displays a typical diffusive trajectory of a single gold nanoparticle with a diameter of 40 nm. The particle was coated by transferrin and bound to transferrin receptors within the plasma membrane of a fibroblast [39]. Each color in Fig. 2 represents the confined diffusion of the nanoparticle within a certain membrane segment until the particle escapes to an adjacent segment where it again undergoes confined diffusion, etc. In this example,

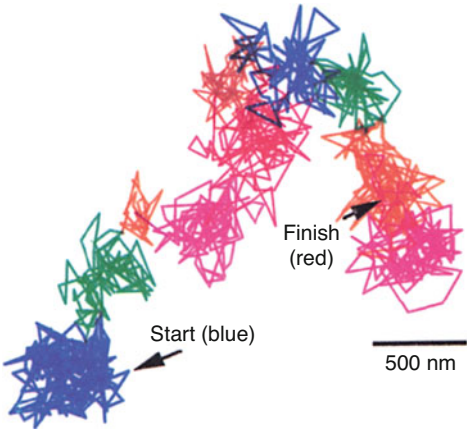

Fig. 2 Diffusive motion of a transferrin-coated gold particle bound to transferrin receptors on the plasma membrane of a fibroblast [39]. The membrane-bound particle undergoes confined diffusion in separate membrane segments, corresponding to the different colors, until it escapes to an adjacent segment. The average size of these segments was 280 nm, the average residence time of the particle in one of these segments was 29 s

the membrane segments had an average radius of 280 nm and the particles remained within one of these segments for an average residence time of 29 s.

The confined diffusion implies that the complex of nanoparticle and receptor molecules encounters some obstacles that prevent its free lateral diffusion. In fact, two types of obstacles have been proposed [40, 42]. First, cytoskeletal proteins that are immobile over the diffusive time scales may act as "corrals" or "fences" for diffusing membrane proteins that have an ectodomain protruding into the cytosol. Second, the cytoskeletal cortex may also directly bind transmembrane proteins and these transiently bound proteins can then act as "rows of pickets" that impede even the diffusion of lipid molecules in the outer leaflet of the bilayer membrane. More recent studies have corroborated the influence of the actin cortex on the lateral diffusion of membrane-anchored receptors. While the diffusion of some receptors was confined to the voids of the actin–myosin meshwork [43, 44], other receptors were observed to undergo quasi-one-dimensional diffusion, reflecting attractive interactions between the latter receptors and the meshwork [45].

3.2 Ambience-Induced Segmentation of Membranes

The skeleton-induced partitioning of cell membranes represents an important but relatively complex example for ambience-induced segmentation of membranes. Much simpler examples are provided by adhering vesicles, hole- or pore-spanning membranes, and membranes supported by chemically patterned surfaces [46, 47].

In these latter systems, the membrane molecules are exposed to two different environments which generate different molecular fields within the adjacent membrane segments. Likewise, vesicle–vesicle adhesion combined with vesicle–substrate adhesion can easily lead to ambience-induced partitioning of a vesicle membrane into more than two segments [48]. For a one-component membrane, the different segments will exhibit different molecular densities which are necessarily small and, thus, difficult to detect experimentally. For a multicomponent membrane, the different segments will also differ in their molecular composition. It then follows from general theoretical considerations that phase domains can only form in one of the membrane segments but not in several segments simultaneously [46, 47].

3.3 Impeded Formation of Intramembrane Domains

The environment of a cell membrane is rather heterogeneous, and the effective molecular fields acting on the membrane molecules change on nanoscopic scales. The skeleton-induced membrane segmentation as probed by single particle tracking (Fig. 2) implies that we can distinguish at least two types of membrane segments, contact segments that interact with the cytoskeletal proteins and noncontact segments that do not experience such interactions. However, different contact segments will, in general, be exposed to cytoskeletal structures that differ in their molecular composition of actin-binding proteins [49, 50] and noncontact segments involve additional supramolecular structures such as the protein scaffolds formed during clathrin-dependent endocytosis that have a lifetime in the range between 20 and 80 s [51, 52]. Thus, cell membranes are expected to be partitioned into many distinct membrane segments that are exposed to different molecular environments. If lipid phase domains form in such a cell membrane, this domain formation is necessarily restricted to one of the membrane segments and, thus, hard to detect [48]. In the limiting case in which the environmental heterogeneities of the cell membrane act as long-lived random fields, these heterogeneities would completely destroy domain formation and phase separation, in analogy to the two-dimensional Ising model with random fields [53–55].

4 Emergence of Membrane Curvature on Nanoscopic Scales

Because of their fluidity, biomembranes are rather flexible and can easily change their shape. Indeed, one fascinating aspect of membranes and vesicles is that they can attain many different nonspherical shapes. When viewed under the optical microscope, these shapes appear to be rather smooth, see the examples in Fig. 1. Therefore, on the micrometer scale, membranes can be described as smoothly curved surfaces and then characterized by their curvature. However, this smoothness does not persist to molecular scales, i.e., when we resolve the molecular structure of a bilayer membrane as in Fig. 3.

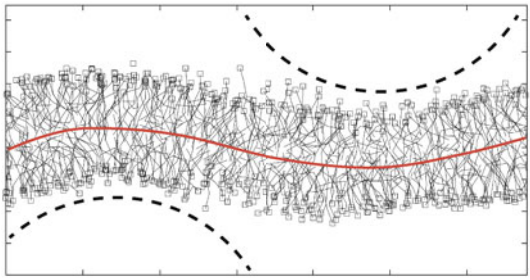

Fig. 3 Emergence of membrane curvature in molecular dynamics simulations of a tensionless membrane [56]. The lipid bilayer has a thickness of about 4 nm, the smallest curvature radius of its midsurface (red) was observed to be about 6 nm. For comparison, two circles (broken lines) with a radius of 6 nm are also displayed

4.1 Basic Aspects of Membrane Curvature

Because membranes are immersed in liquid water, each lipid and protein molecule undergoes thermal motion with displacements both parallel and perpendicular to the membrane. The perpendicular displacements represent molecular protrusions that roughen the two interfaces bounding the membrane, see Fig. 3. Therefore, in order to characterize a lipid/protein bilayer by its curvature, one has to consider small membrane patches and to average over the molecular conformations within these patches. The minimal lateral size of these patches can be determined from the analysis of the bilayer's shape fluctuations and was found, from molecular dynamics simulations of a one-component lipid bilayer, to be about 1.5 times the membrane thickness, see Fig. 3 [56]. For a membrane with a thickness of 4 nm, this minimal size is about 6 nm. Because such a membrane patch contains 80–100 lipid molecules, membrane curvature should be regarded as an emergent property arising from the collective behavior of a large number of lipid molecules.

4.2 Tensionless States of Membranes

The curvature just discussed applies to the midsurface of the bilayer membrane, i.e., to the surface between the two leaflets of the bilayer. Furthermore, for a membrane segment with midsurface area A and bending rigidity κ, curved conformations as in Fig. 3 are only possible if the membrane is "tensionless" in the sense that the mechanical membrane tension as obtained from the stress profile across the bilayer [57] is small compared to κ/A. For the example displayed in Fig. 3, the latter tension scale is found to be $\kappa/A = 0.08\,\mathrm{mN/m}$. Such tensionless states, which represent the natural reference states of the membranes, can be used to determine the bending rigidity from the undulation spectrum [56, 58–60] and the Gaussian

curvature modulus from the stress profile [61, 62], and the spontaneous curvature induced by the interactions with small solutes such as ions or monosaccharides [63, 64]. Attractive interactions between the solutes and the membrane lead to adsorption layers adjacent to the two leaflets, repulsive interactions to depletion layers. The spontaneous curvatures generated by depletion and adsorption have opposite signs [65]. Furthermore, both attractive and repulsive membrane-solute interactions generate a spontaneous curvature that varies linearly with the solute concentration difference between the exterior and interior solution [63, 64], in agreement with our analytical theories.

4.3 Simulations of More Complex Membrane Processes

During the last 20 years, molecular simulations of membranes have become a rather popular tool. Indeed, up to 1995, about 300 publications had been published on the molecular dynamics of membranes but, during the last 20 years, the same topic was addressed in about 25,000 publications. Using such simulations, one can study molecular remodelling processes such as membrane fusion [66–70] or membrane adhesion via membrane-anchored receptors and ligands [71–73]. In addition, simulation snapshots provide useful insights into the typical molecular conformations of the membrane systems and allow to compare the free energies of different conformations. One recent example is provided by the adsorption of PEG molecules onto liquid-ordered and liquid-disordered membranes [74].

5 Local Curvature Generation and Spontaneous Curvature

During the 1990s, I thought about a variety of ways to generate membrane curvature locally by membrane-bound macromolecules and adhesive nanoparticles. One simple example is provided by a flexible polymer that is anchored with one of its ends to the membrane, see Fig. 4a [75, 76]. Such an anchored polymer generates curvature by entropic forces because it can increase its configurational entropy by curving the membrane away from it. Another simple example are adhesive nanoparticles that are partially engulfed by the membrane, see Fig. 4b [34, 65, 77]. Here, the rigid particle imposes the curvature of its surface directly onto the membrane provided that the particle size is large compared to the membrane thickness. Curvature can also be generated by the adsorption of nanoparticles that are small compared to the membrane thickness, see Fig. 4c [65, 78]. In fact, small adhesive solutes with a diameter below 1 nm can generate spontaneous curvatures as large as 1/(20 nm) as recently shown by molecular dynamics simulations [63]. In these simulations, the adsorbed solutes increased the molecular area per lipid. The opposite effect is also possible, arising from the condensation of the lipid head groups. The two effects lead to opposite signs of the spontaneous curvature as proposed for the adsorption of calcium cations onto negatively charged membranes [80, 81].

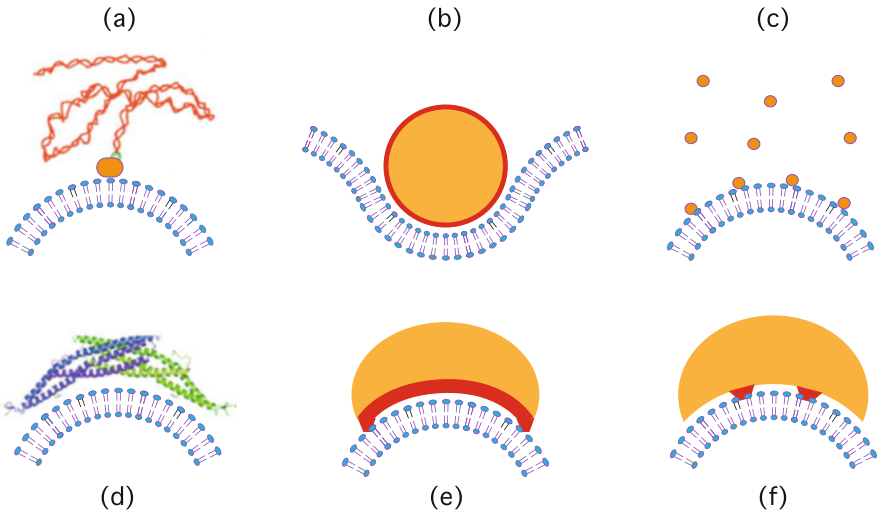

Fig. 4 Different mechanisms for local generation of membrane curvature: (**a**) Flexible polymer with one end anchored to the membrane [75] such as biotinylated DNA (red) linked to membrane-anchored avidin (orange) [76]; (**b**) spherical nanoparticle (orange) with an adhesive surface (red) partially engulfed by the membrane [34, 65, 77]. The particle radius is about 2.5 times the membrane thickness; (**c**) asymmetric adsorption of solutes that are small compared to the membrane thickness [63, 65, 78]; (**d**) N-BAR-domain protein with a curvature radius of about 11 nm [79] bound to the membrane; (**e**) BAR-mimetic nanoparticle with a large adhesive surface domain (red) that generates curvature via an induced-fit mechanism; and (**f**) BAR-mimetic nanoparticle with relatively small adhesive surface domains (red) which generate curvature via conformational selection [48]. Note that the sign of the local curvature in (**b**) is opposite to the sign of the local curvature in all other panels

5.1 Local Curvature Generated by Membrane-Bound Proteins

At the end of the 1990s, several labs started to use a simple experimental criterion to assess the curvature-generating capabilities of certain proteins. This criterion was based on the transformation of liposomes into tubular structures via protein adsorption and was used to identify, in a qualitative manner, a variety of curvature-generating proteins: N-BAR proteins such as amphiphysin [79] and endophilin [82], see Fig. 4d, F-BAR proteins such as pacsin/syndapin [83], and other proteins involved in endocytosis such as epsin [84]. The discovery of proteins that generate membrane curvature provides another rather interesting connection between biophysics and molecular cell biology.

The membrane-binding proteins are usually quite rigid and can be regarded as adhesive nanoparticles with two characteristic properties: (i) their shape is typically nonspherical and often banana-like or convex–concave; and (ii) their surface contains a more or less complex pattern of adhesive and nonadhesive surface domains. Thus, the membrane-binding proteins can be regarded as nonspherical

Janus-like nanoparticles. If the planar membrane can bind to some of the adhesive surface domains of the protein, this protein generates membrane curvature via an induced-fit mechanism, see Fig. 4e. In contrast, if the adhesive surface domains can only be reached by an appropriately curved membrane as in Fig. 4f, the protein senses and stabilizes membrane curvature via conformational selection [48].

5.2 From Local to Spontaneous Curvature

If the membrane is decorated by many bound solutes or "particles," it will acquire a certain spontaneous curvature that depends both on the local particle-induced curvature and on the particle coverages on the two leaflets of the bilayer membrane [85, 86]. Thus, if a single particle that is bound to the outer leaflet of the bilayer induces the local curvature M_1 in a membrane patch of area A_1, the spontaneous curvature m is given by

$$m = A_1 M_1 (\Gamma_{\rm ex} - \Gamma_{\rm in}) \tag{1}$$

where the coverages $\Gamma_{\rm ex}$ and $\Gamma_{\rm in}$ are defined by the numbers of particles bound to the outer and inner leaflets per unit area. The product $A_1 M_1 = \int dA\, M_{\rm si}$ can be determined by first calculating the local, position-dependent mean curvature $M_{\rm si}$ as generated by a single particle bound to the outer leaflet of an asymptotically flat membrane [85]. In contrast to other elastic membrane parameters such as the bending rigidity or the area compressibility modulus, the spontaneous curvature can vary over more than three orders of magnitude, from the inverse size of giant vesicles, which is of the order of $1/(50\,\mu{\rm m})$, to half the inverse membrane thickness, which is of the order of $1/(10\,{\rm nm})$.

5.3 Short History of Spontaneous Curvature

The spontaneous (or preferred) curvature m considered here describes the local bilayer asymmetry arising from the intermolecular interactions. Such a curvature was first discussed by Bancroft for surfactant monolayers in water–oil emulsions [87, 88]. It was also included by Frank, as the so-called splay term, in his theory for the curvature elasticity of liquid crystals [89]. In the context of lipid bilayers, spontaneous curvature as a local elastic parameter was first considered by Helfrich [90], in analogy to the liquid crystal case. The corresponding bending energy of the membrane is now known as the spontaneous curvature model [91].

If the membrane molecules cannot undergo flip-flops between the two leaflets, the number of molecules is fixed within each leaflet, and the quenched difference between these two numbers leads to a preferred area difference between the leaflets. This constraint was originally considered by Evans [92], incorporated

into the bilayer-coupling model of Svetina and Zeks [91, 93], and generalized in terms of the area-difference-elasticity model by Wortis and coworkers [94, 95]. As shown in these latter studies, the stationary shapes of the area-difference-elasticity model are also stationary shapes of the spontaneous curvature model provided that one defines an effective spontaneous curvature that includes a nonlocal, shape-dependent contribution. The latter contribution can be calculated explicitly for limit shapes that consist of two spherical membrane segments connected by a closed membrane neck [2]. Furthermore, the constraints on the area difference should be irrelevant if the bilayer membranes contain molecules such as cholesterol that can easily undergo flip-flops and, thus, relax local stresses induced by the bending deformations [96, 97]. In addition, even in the absence of flip-flops, the area-difference-elasticity term represents a small correction term whenever the (local) spontaneous curvature m is large compared to the inverse vesicle size. The latter separation of length scales applies, in particular, to the processes of nanotube formation and particle engulfment as considered in the following.

5.4 Sign of Spontaneous Curvature

It is important to note that the spontaneous curvature can be positive or negative. Within the spontaneous curvature model, the energy density of a membrane segment is proportional to $(M - m)^2$ which depends on the mean curvature M of this segment. It then follows that the spontaneous curvature is positive (negative) if the segment prefers to attain a positive (negative) mean curvature M. Furthermore, we need a convention to distinguish the two possible signs of the mean curvature in a unique manner. Here and below, I use the convention that the mean curvature M of a membrane segment is *positive* if it bulges towards the *exterior* aqueous compartment and negative if it bulges towards the interior compartment. Thus, if the exterior compartment in Fig. 4 is located on top of the membrane segments, the mean curvature of these segments is positive for panels (a) and (c)–(f) but negative for panel (b).

6 Two Mechanisms for the Formation of Membrane Nanotubes

Now, consider a membrane segment with area A and assume that this segment has a spontaneous curvature m that is large compared to $1/\sqrt{A}$. The membrane can then minimize its free energy by forming a long tube with a diameter of the order of $1/|m|$. More precisely, it may form a necklace-like tube consisting of small spheres with radius $1/|m|$, connected by closed membrane necks, a cylindrical tube with radius $1/(2|m|)$, or unduloids that interpolate between the necklace and the cylinder [74, 78].

6.1 Spontaneous Tubulation of Membranes

Recent experimental studies on supported lipid bilayers and giant vesicles have indeed shown that unilamellar membrane systems can undergo spontaneous tubulation, i.e., can form membrane tubules or nanotubes without the application of external forces. In the case of supported lipid bilayers, the tube formation was induced by the adsorption of antimicrobial peptides [98, 99]. In the case of giant vesicles, spontaneous tubulation was observed for a variety of binary and ternary lipid mixtures when the two leaflets of the vesicle membrane were exposed to aqueous polymer solutions that differed in their composition [74, 100].

Depending on the phase behavior of the aqueous polymer solution, the GUV membranes form different patterns of flexible nanotubes as shown in Fig. 5 for the liquid-disordered phase of a three-component membrane. All tubes were observed to be in-tubes protruding into the interior of the vesicles. For the liquid-disordered membranes, the morphology of the tubes could not be resolved because the tube diameter was below the optical diffraction limit. However, short and long tubes are theoretically predicted to be necklace-like and cylindrical, respectively [74].

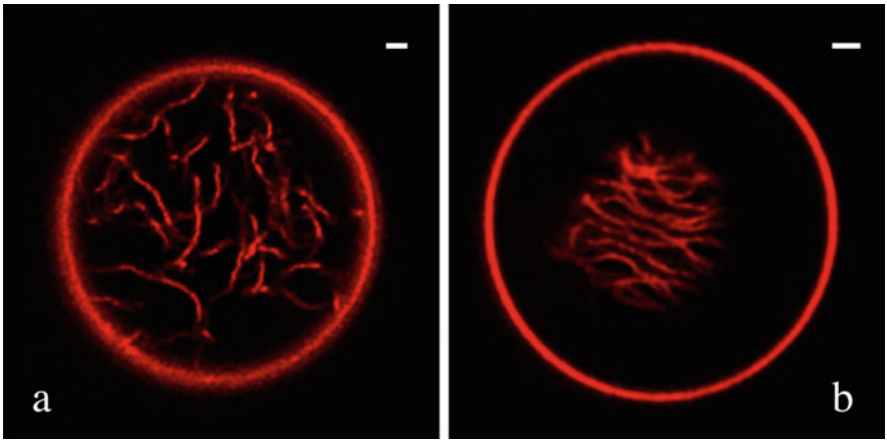

Fig. 5 Patterns of flexible nanotubes formed by liquid-disordered membranes exposed to aqueous solutions of PEG and dextran. All tubes are in-tubes in the sense that they protrude into the vesicle interior: (**a**) Disordered pattern of in-tubes freely suspended within the PEG-rich droplet enclosed by the vesicle; and (**b**) Thin layer of tubes adhering to the interface between the PEG-rich and the dextran-rich phase, with some short-range orientational order arising from crowding. The diameter of the tubes is below the diffraction limit but the tubes are theoretically predicted to be necklace-like and cylindrical in panels (**a**) and (**b**), respectively [74]. Scale bars: 2 μm

6.2 Necklace-to-Cylinder Transformation of Nanotubes

In fact, according to our theory, the tubes undergo a novel shape transformation from necklace-like to cylindrical tubes at a certain critical tube length, consistent with experimental observations for liquid-ordered membranes. Using the parameters of the liquid-disordered membranes, the tubes in Fig. 5a, b are predicted to be necklace-like and cylindrical, respectively. Furthermore, the spontaneous curvature of all tubes shown in Fig. 5 is about 1/(125 nm) as deduced via three distinct and independent methods of image analysis [74].

The presence of a necklace–cylinder transformation at a critical tube length can be understood as follows. Both the necklace-like tube and the main body of the cylindrical tube have zero bending energy. The two endcaps of the cylindrical tube contribute a bending energy of the order of $2\pi\kappa$. Therefore, the bending energy of the membrane disfavors the cylindrical tube. On the other hand, the necklace-like tube has a larger volume compared to the cylindrical one and the osmotic pressure difference across the membranes acts to compress the tubes when they protrude into the interior of the vesicles. Therefore, such an in-tube can lower its energy by reducing its volume which favors the cylindrical tube. The volume work is proportional to the tube length whereas the bending energy of the endcaps is independent of this length. It then follows from the competition between these two energies that short tubes are necklace-like whereas long tubes are cylindrical. Using superresolution microscopy such as STED, it should be possible to directly resolve the tube morphologies underlying the tube patterns in Fig. 5.

6.3 Increased Robustness of Tubulated Vesicles

The nanotubes arising from spontaneous tubulation provide the mother vesicle with a large reservoir of membrane area. Therefore, the mother vesicle can respond to mechanical perturbations by exchanging area with the tubes and then behaves much like a liquid droplet with variable surface area. This increased mechanical robustness of the mother vesicle has been recently demonstrated by micropipette aspiration [101]. The initial aspiration for small suction pressure directly reveals the spontaneous tension [78]

$$\sigma \equiv 2\kappa m^2 \tag{2}$$

of the vesicle membranes which represents the intrinsic tension scale of a membrane with bending rigidity κ and spontaneous curvature m. When the suction pressure reaches a σ-dependent critical value, the tubulated vesicles start to flow into the micropipette, thereby behaving like liquid droplets with an effective interfacial tension that is provided by the spontaneous tension σ [101].

6.4 Force-Induced Tubulation of Membranes

A second, quite different mechanism for the formation of membrane nanotubes is provided by external forces that are locally applied to the membranes of cells and giant vesicles. In order to generate such forces, one has to "grab" the cell or vesicle, e.g., by an adhesive surface or by a micropipette, and then apply some localized force which often acts onto a membrane-bound bead or nanoparticle. A variety of such force-generating methods have been used over the years: hydrodynamic flow applied to adhering cells [102–104], aspirated cells [105, 106], aspirated vesicles [107, 108], and vesicles attached to the tip of a micro-rod [109]; relative displacement of two micropipettes, one of which holds a membrane-bound bead while the other aspirates a cell [105] or GUV [110, 111]; gravity acting on a bead attached to an aspirated vesicle [112]; laser traps acting on a bead attached to cells [113–115], aspirated vesicles [80, 116, 117], and adhering vesicles [118]; as well as magnetic tweezers acting on a bead bound to aspirated vesicles [119] and adhering cells [120]. In addition, networks of membrane tubules have been generated by molecular motors moving along microtubules [121–124] as well as by manipulating adhering vesicles by micropipettes [125, 126]. A particularly instructive set-up for force-induced tubulation is provided by micropipette aspiration of a GUV combined with a membrane-bound nanobead to which one can apply a pulling force f via magnetic tweezers [119] or optical traps [80, 116, 117], as schematically depicted in Fig. 6. This set-up will now be considered in order to discuss the interplay between spontaneous and force-induced tubulation in a quantitative manner.

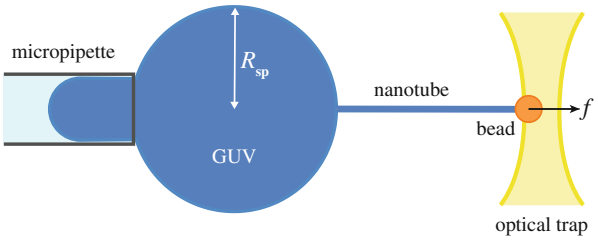

Fig. 6 Pulling a membrane nanotube attached to a bead from a giant unilamellar vesicle (GUV) by an optical trap: The weakly curved GUV is aspirated by the micropipette; the right end of the strongly curved nanotube experiences the pulling force f arising from the optical trap. The force f is taken to be positive for an out-tube as shown here and negative for an in-tube

7 Interplay Between Spontaneous and Force-Induced Tubulation

7.1 Tube Width Determined by Composite Curvature

In general, the diameter of a membrane nanotube depends both on the spontaneous curvature m and on the pulling force f [78]. It will be convenient to take the force f to be positive and negative if it points towards the exterior and interior aqueous solution, respectively (this convention is different from the one used in [78], where f described the absolute value of the pulling force for both pulling directions). To be specific, let us consider a cylindrical out-tube that protrudes from a GUV with a large spherical segment of radius $R_{\rm sp}$ as in Fig. 6. We can then distinguish different parameter regimes depending on the relative magnitudes of the composite curvature

$$m_{\rm com} \equiv m + \frac{f}{4\pi\kappa} \quad \text{and } 1/R_{\rm sp}. \tag{3}$$

The composite curvature $m_{\rm com}$ represents the superposition of the spontaneous curvature m with the rescaled pulling force $f/(4\pi\kappa)$ and directly describes the interplay of the two tubulation mechanisms. Indeed, the composite curvature can be positive or negative depending on the sign of m and f. As mentioned before, I use the sign convention that the spontaneous curvature m of a membrane segment is positive if this segment prefers to bulge towards the exterior compartment.

If the composite curvature is positive and much larger than the inverse vesicle radius, i.e., if $m_{\rm com} \gg 1/R_{\rm sp}$, the vesicle membrane can form cylindrical out-tubes with the mean curvature [78]

$$M_{\rm cy} \approx m_{\rm com} - \frac{1}{4R_{\rm sp}} = m + \frac{f}{4\pi\kappa} - \frac{1}{4R_{\rm sp}} \tag{4}$$

for small values of $1/(R_{\rm sp}\, m_{\rm com})$ as follows from the Euler–Lagrange equation (or shape equation) of the spontaneous curvature model and the force balance at the tube end.[1] Here and below, the symbol $\approx$ stands for "asymptotically equal" in the limit in which a certain parameter becomes small (or large). The relation (4) also applies to cylindrical in-tubes which form for negative composite curvatures with

[1] More precisely, the relation (4) is obtained for the mechanical equilibrium between a spherical membrane segment with mean curvature $M_{\rm sp} = 1/R_{\rm sp}$ and a cylindrical segment with mean curvature $M_{\rm cy}$, coexisting on the same vesicle, by combining the two Euler–Lagrange equations for these membrane segments with the force balance at the tube end, see [78].

$m_{\rm com} \ll -1/R_{\rm sp}$. In both cases, the tube radius is given by

$$R_{\rm cy} \approx \frac{1}{2|m_{\rm com}|} = \frac{1}{\left|2m + \frac{f}{2\pi\kappa}\right|} \quad \text{for } |m_{\rm com}| \gg 1/R_{\rm sp}. \tag{5}$$

Thus, in this parameter regime, the tube radius $R_{\rm cy}$ is directly determined by the composite curvature $m_{\rm com}$, i.e., by the combined action of the two tubulation mechanisms provided by spontaneous curvature m and pulling force f. If m and f have the same sign, these two mechanisms act synergistically whereas they act antagonistically if m and f have opposite sign. In both cases, the radius is primarily determined by the spontaneous curvature in the parameter regime with $|m| \gg |f|/(4\pi\kappa)$ and by the pulling force for $|f| \gg 4\pi\kappa|m|$.

7.2 Composite Curvature and Total Membrane Tension

The mechanical equilibrium between a cylindrical tube and a large spherical mother vesicle [78] also implies the relation

$$m_{\rm com} = m + \frac{f}{4\pi\kappa} \approx \pm\left(\frac{\hat{\Sigma}}{2\kappa}\right)^{1/2} - \frac{1}{4R_{\rm sp}} \quad \text{for large } R_{\rm sp}/R_{\rm cy} \tag{6}$$

where the plus and minus sign applies to out- and in-tubes, respectively, with the total membrane tension

$$\hat{\Sigma} \equiv \Sigma + \sigma = \Sigma + 2\kappa m^2 \tag{7}$$

which represents the superposition of the mechanical tension Σ and the spontaneous tension σ as defined in (2).

It has been recently shown that it is possible to pull both out- and in-tubes via an optical trap from the same aspirated GUV [108, 127]. One can then measure the two forces $f_{\rm ex}$ and $f_{\rm in}$ that generate out- and in-tubes for the same aspiration pressure. Both cases are described by (6) with f replaced by $f_{\rm ex}$ for the plus sign and by $f_{\rm in}$ for the minus sign. The sum of these two relations leads to the simple expression

$$m \approx -\frac{f_{\rm ex} + f_{\rm in}}{8\pi\kappa} - \frac{1}{4R_{\rm sp}} \tag{8}$$

for the spontaneous curvature m. In this way, one can determine the spontaneous curvature m by force-induced tubulation regardless of the membrane tension. For symmetric bilayers as studied in [108], the spontaneous curvature vanishes and the relation (8) implies that $f_{\rm in} = -f_{\rm ex}$. For GUVs containing a binary mixture of POPC and GM1, on the other hand, the out- and in-pulling forces, $f_{\rm ex}$ and $f_{\rm in}$, were observed to have different magnitudes, i.e., $f_{\rm in} \neq -f_{\rm ex}$ which implies a nonzero spontaneous curvature [127].

7.3 Total Membrane Tension Versus Aspiration Tension

The relationship between the composite curvature and the total membrane tension as given by (6) involves the total membrane tension $\hat{\Sigma}$ defined in (7). In some experimental studies, [80, 117] the relation (6) was used with the total membrane tension replaced by the aspiration tension

$$\Sigma_{\rm asp} \equiv \frac{(P_{\rm ex} - P_{\rm pip})R_{\rm pip}}{2(1 - R_{\rm pip}/R_{\rm sp})} \,. \tag{9}$$

which can be directly obtained from measured values of the suction pressure $P_{\rm ex} - P_{\rm pip}$ of the micropipette and the radii $R_{\rm pip}$ and $R_{\rm sp}$ of the pipette and the nonaspirated membrane segment. The expression (9) follows from the Laplace equation for the spherical endcap of the fully aspirated membrane tongue with mean curvature $M_{\rm cap} = 1/R_{\rm pip}$, see, e.g., [128]. However, the Laplace equation represents a truncation of the full Euler–Lagrange (or shape equation) for a spherical membrane segment. As a consequence, the total membrane tension $\hat{\Sigma}$ in (6) is not equal to the aspiration tension $\Sigma_{\rm asp}$ but satisfies, for $M_{\rm cap} = 1/R_{\rm pip}$, the more general relation

$$\hat{\Sigma} = \Sigma_{\rm asp} + \Delta\hat{\Sigma} \tag{10}$$

with the additional tension term

$$\Delta\hat{\Sigma} \equiv 2\kappa m \left(\frac{1}{R_{\rm pip}} + \frac{1}{R_{\rm sp}}\right) . \tag{11}$$

As an example, let us consider a GUV membrane with bending rigidity $\kappa = 10^{-19}$ J and spontaneous curvature $m = \tilde{m}/\mu$m. Let us further assume that the GUV is aspirated by a micropipette of radius $R_{\rm pip} = 3\,\mu$m and that the nonaspirated membrane segment forms a spherical segment of radius $R_{\rm sp} = 6\,\mu$m. The additional tension term $\Delta\hat{\Sigma}$ then has the magnitude $0.1\tilde{m}\,\mu$N/m which is equal to $1\,\mu$N/m for $\tilde{m} = 10$ or $m = 1/(100\,{\rm nm})$. The magnitude of $\Delta\hat{\Sigma}$ should be compared to the smallest values of the aspiration tension which are also of the order of $1\,\mu$N/m for the considered geometry, corresponding to the smallest accessible suction pressures of about 1 Pa. Therefore, we conclude that the additional tension term $\Delta\hat{\Sigma}$ can only be ignored for suction pressures that are much larger than 1 Pa and for spontaneous curvatures m that are much smaller than $1/(100\,{\rm nm})$.

7.4 Different Parameter Regimes

As emphasized before, both the spontaneous curvature m and the pulling force f can be positive or negative. Irrespective of the signs of m and f, the expressions (4)–(6)

are valid as long as $\left|m + \frac{f}{4\pi\kappa}\right| \gg 1/R_{\rm sp}$. The latter inequality is not fulfilled: (i) if both $|m|$ and $|f|/(4\pi\kappa)$ are smaller than or comparable to the inverse vesicle radius $1/R_{\rm sp}$ or (ii) if m and $f/(4\pi\kappa)$ have opposite sign and (almost) cancel each other. In case (i), the vesicle membrane cannot form nanotubes at all. In case (ii), nanotubes are still possible but only if the curvature ratio $|m|/M_{\rm sp} = |m|R_{\rm sp} \gtrsim 10^3$. In the latter case, the mean curvature of the tube behaves as $M_{\rm cy} \approx \pm(|m|M_{\rm sp}^2/4)^{1/3}$ and, thus, depends strongly on the vesicle size as follows from the theory in [78]. The different regimes for the interplay between spontaneous and force-induced tubulation can be probed experimentally by first pulling a tube from a GUV membrane with no spontaneous curvature and subsequently generating a positive or negative spontaneous curvature in this membrane, e.g., by adsorption of macromolecules or nanoparticles.

8 Engulfment of Nanoparticles by Membranes

One process for which the spontaneous curvature represents a key parameter is the engulfment of nanoparticles by membranes [34]. These particles are widely used to deliver drugs, imaging agents, and toxins to biological cells [129–131]. The cellular uptake of such a particle requires the adhesion of this particle to the cell membrane and its subsequent engulfment by this membrane, a process that is governed by the competition between particle adhesion and membrane bending [34, 65, 77]. The same process is misused by viruses that enter the host cell by receptor-mediated endocytosis and by enveloped viruses that exit the host cell by exocytosis.

8.1 Nanoparticles in Contact with Membranes

An adhesive nanoparticle that comes into contact with a membrane can remain in a free, nonadhering state or can become engulfed by the membrane. In the latter case, the membrane may cover only part of the particle surface or engulf the particle completely. These three different states of the nanoparticle are illustrated in Fig. 7. In order to understand the energetics of these states, it is rather instructive to consider the stability (i) of the free state against the onset of membrane spreading and (ii) of the completely engulfed state against the opening of the closed membrane neck. This stability analysis can be performed in a systematic manner and leads to two relatively simple stability relations [34] which have a number of interesting consequences [132–134] as briefly summarized in the following subsections.

The stability of the free, nonadhering state in Fig. 7a depends only on three parameters: the mean curvature M of the membrane segment that comes into contact with the particle, see Fig. 7a; the particle size $R_{\rm pa}$; and the adhesion length

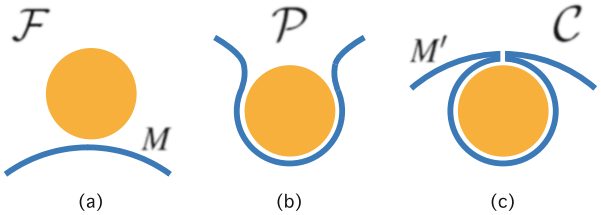

Fig. 7 Three possible states of a nanoparticle (orange) in contact with a membrane segment (blue): (**a**) free, nonadhering state $\mathscr{F}$ in which the membrane does not spread over the particle surface in spite of the attractive membrane–particle interactions; (**b**) partially engulfed state $\mathscr{P}$ in which the membrane covers some part of the particle surface; and (**c**) completely engulfed state $\mathscr{C}$ in which the membrane covers the whole particle surface and forms a closed neck that connects the bound membrane segment to the unbound membrane of the mother vesicle. The particles originate from the exterior aqueous solution corresponding to endocytic engulfment. The membrane segment in (**a**) has mean curvature M, and the unbound membrane segment in (**c**) has mean curvature M'. All bound membrane segments have the mean curvature $-1/R_{\rm pa}$ [34]

$$R_W \equiv \sqrt{2\kappa/|W|} \tag{12}$$

which represents a material parameter that is independent of the membrane geometry and encodes the competition between the bending rigidity κ of the membrane and the adhesive strength $|W|$ of the membrane–particle interactions [135]. Depending on the chemical composition of the membrane and the nanoparticle, the adhesion length R_W can vary from about 10 nm for strong adhesion to a couple of micrometers for ultra-weak adhesion [34]. The adhesion length R_W provides the basic length scale for engulfment processes and the most interesting engulfment behavior is found for nanoparticle sizes of the order of R_W.

8.2 *(In)stability of Free Particle State and Onset of Adhesion*

To be specific, consider the endocytic engulfment of spherical nanoparticles of radius $R_{\rm pa}$ dispersed in the exterior aqueous compartment. When such a particle comes close to a membrane segment with mean curvature M,[2] this segment does *not* adhere to the particle, even in the presence of attractive membrane–particle interactions, if [34, 132]

$$M \geq M_{\rm fr} \equiv -\frac{1}{R_{\rm pa}} + \frac{1}{R_W} \quad \text{(no adhesion, endocytic process)}, \tag{13}$$

[2] As explained before, the mean curvature M of a membrane segment is taken to be positive (negative) if this segment bulges towards the exterior (interior) compartment.

i.e., if the membrane's mean curvature M exceeds the threshold value $M_{\rm fr}$ that depends on the particle radius and the adhesion length. The stability criterion (13) implies that the free, nonadhering particle state is stable for all particle sizes if the membrane curvature $M \geq 1/R_W$, i.e., a membrane segment with a sufficiently large positive curvature M does not start to spread onto a particle of any size. Note that the threshold value $M_{\rm fr}$ is independent of the spontaneous curvature m of the membrane, which is somewhat counterintuitive. On the other hand, if the mean curvature is below this threshold value and within the range [34, 132]

$$-\frac{1}{R_{\rm pa}} < M < M_{\rm fr} = -\frac{1}{R_{\rm pa}} + \frac{1}{R_W} \quad \text{(onset of adhesion, endocytic process)}, \tag{14}$$

the membrane segment starts to spread over the particle surface. The first inequality $-1/R_{\rm pa} < M$ ensures that membrane segment and particle can come into direct contact without intersecting each other, compare Fig. 8c1. Note that the curvature range as given by (14) becomes rather small if the adhesion length R_W is large compared to the particle size $R_{\rm pa}$. In such a situation, one has to fine-tune the parameters in order to observe the onset of adhesion experimentally. The stability relations (13) and (14) are illustrated in Fig. 8a–c.

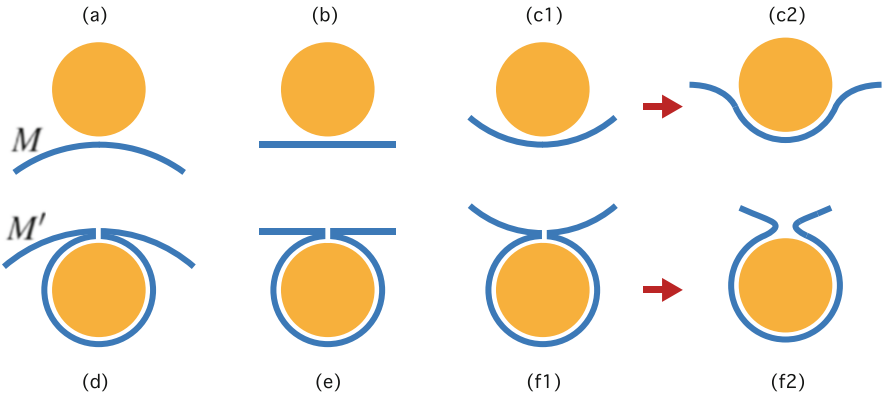

Fig. 8 Endocytic engulfment of nanoparticles (orange) originating from the exterior solution: (**a**)–(**c**) The top row illustrates the (in)stability of the free, nonadhering particle state for curvature threshold $M_{\rm fr} = 0$, see (13) and (14). The free state is stable in (**a**) with membrane curvature $M > 0$, marginally stable in (**b**) with $M = 0$, and unstable in (**c1**) with $M < 0$. The instability of (**c1**) leads to the onset of adhesion and to the partially engulfed state in (**c2**). (**d**)–(**f**) The bottom row illustrates the (in)stability of the completely engulfed state with a closed membrane neck for curvature threshold $M_{\rm ce} = 0$, see (16) and (15). The latter state is stable in (**d**) with curvature $M' > 0$ of the unbound membrane, marginally stable in (**e**) with curvature $M' = 0$, and unstable in (**f1**) with $M' < 0$. The instability of (**f1**) leads to an opening of the membrane neck and to the partially engulfed state in (**f2**)

8.3 (In)stability of Completely Engulfed Particle State

The stability of the completely engulfed state in Fig. 7c depends on four parameters: in addition to the three parameters that are also relevant for the onset of adhesion, the stability of the completely engulfed state depends on the spontaneous curvature m as well. Now, consider a completely engulfed state with a closed membrane neck that connects the bound membrane segment in contact with the nanoparticle to the adjacent segment of the unbound vesicle membrane. The latter membrane segment has the mean curvature M' as in Fig. 7c. The closed membrane neck starts to open up if M' satisfies the inequality [34, 132]

$$M' < M_{\rm ce} \equiv 2m + \frac{1}{R_{\rm pa}} - \frac{1}{R_W} \quad \text{(neck opening, endocytic process)}, \tag{15}$$

i.e., if the mean curvature M' is below the threshold value $M_{\rm ce}$ that depends on the spontaneous curvature, the particle size, and the adhesion length. The instability criterion (15) implies that the completely engulfed state is unstable for all particle sizes if the membrane curvature $M' < 2m - 1/R_W$ which is always fulfilled for a sufficiently large negative value of M'. On the other hand, the closed neck is stable if the curvature M' is above the threshold value $M_{\rm ce}$ and within the range [34, 132]

$$M_{\rm ce} = 2m + \frac{1}{R_{\rm pa}} - \frac{1}{R_W} \le M' < \frac{1}{R_{\rm pa}} \quad \text{(closed neck, endocytic process)}. \tag{16}$$

The last inequality $M' < 1/R_{\rm pa}$ ensures that the vesicle membrane and the particle do not intersect each other.

In biological cells, many processes that lead to the formation of membrane buds with closed necks involve proteins that generate constriction forces onto the necks [133]. In the case of endocytosis, proteins such as dynamin [136] or ESCRTs [38, 137, 138] are typically involved in neck closure and fission. In phagocytic engulfment by macrophages, a contractile ring composed of actin and myosin motors is formed around the neck [139]. Now, if a spherical nanoparticle with radius $R_{\rm pa}$, adhering to the outer leaflet of the vesicle membrane, is fully engulfed by the membrane, the bound membrane segment forms a spherical bud with mean curvature $M_{\rm bud} = -1/R_{\rm pa}$. In the presence of a radial constriction force $f > 0$ that acts to decrease the neck radius, the closed neck is stable if [133]

$$f + f_{\rm eng} \ge 0 \quad \text{with} \quad f_{\rm eng} \equiv 4\pi\kappa \left(M' + M_{\rm bud} + \frac{1}{R_W} - 2m \right) \tag{17}$$

which generalizes the stability condition (16) and describes the enhanced neck stability in the presence of constriction forces.

Table 1 The (in)stabilities of the free state $\mathscr{F}$ and the completely engulfed state $\mathscr{C}$ as described by the (in)stability conditions (13)–(16) define four engulfment regimes $\mathscr{F}_{\rm st}$, $\mathscr{C}_{\rm st}$, $\mathscr{B}_{\rm st}$, and $\mathscr{P}_{\rm st}$

State $\mathscr{F}$	Stable	Unstable	(Meta)stable	Unstable
State $\mathscr{C}$	Unstable	Stable	(Meta)stable	Unstable
Regime	$\mathscr{F}_{\rm st}$	$\mathscr{C}_{\rm st}$	$\mathscr{B}_{\rm st}$	$\mathscr{P}_{\rm st}$

8.4 Engulfment Regimes of Single Nanoparticles

When we combine the (in)stability conditions for the free particle states $\mathscr{F}$ as given by (13) and (14) with the (in)stability conditions for the completely engulfed particle states $\mathscr{C}$ as described by (15) and (16), we obtain four combinations which define four different engulfment regimes, $\mathscr{F}_{\rm st}$, $\mathscr{C}_{\rm st}$, $\mathscr{B}_{\rm st}$, and $\mathscr{P}_{\rm st}$, as summarized in Table 1.

First, the engulfment regime $\mathscr{F}_{\rm st}$ corresponds to a stable free state $\mathscr{F}$ and an unstable completely engulfed state $\mathscr{C}$ as described by the combination of (13) and (15). Second, the complete engulfment regime $\mathscr{C}_{\rm st}$ is defined by an unstable state $\mathscr{F}$ and a stable state $\mathscr{C}$, i.e., by the combination of (14) and (16). Third, if both the free and the completely engulfed states are stable, one has to combine the stability relations (13) and (16) which leads to the bistable engulfment regime $\mathscr{B}_{\rm st}$. Finally, the partial engulfment regime $\mathscr{P}_{\rm st}$ is obtained by combining the instability conditions (14) and (15) corresponding to the situation in which both the free and the completely engulfed states are unstable.

The (in)stability conditions as given by (13)–(16) depend on the local mean curvatures M and M', which characterize the membrane geometry close to the nanoparticle, see Fig. 7, and on three material parameters, the particle size $R_{\rm pa}$, the adhesion length R_W, and the spontaneous curvature m. In fact, close inspection of these (in)stability conditions reveals that they depend on particle size and adhesion length only via the contact mean curvature $M_{\rm co} \equiv 1/R_W - 1/R_{\rm pa}$. Furthermore, in the small particle limit, i.e., if the nanoparticles are much smaller than the vesicle size, one may identify the local mean curvatures M and M' [132, 134]. In this limit, one is left with a three-dimensional parameter space defined by the local mean curvature M, the contact mean curvature $M_{\rm co}$, and the spontaneous curvature m. The different engulfment regimes can then be visualized by two-dimensional sections through the three-dimensional parameter space [34, 132, 134, 140].

8.5 Engulfment Regimes and Local Energy Landscapes

The (in)stability relations as given by (13)–(16) are intimately related to the local energy landscapes for engulfment as a function of an appropriate reaction coordinate. Convenient reaction coordinates are the wrapping angle for axisymmetric engulfment geometries [34, 77] and the area fraction of the membrane-covered particle surface for non-axisymmetric geometries [133]. The engulfment regimes

$\mathscr{F}_{\rm st}$ are characterized by local energy landscapes with a single minimum at the free state $\mathscr{F}$ and a single maximum at the completely engulfed state $\mathscr{C}$. Likewise, the complete engulfment regime $\mathscr{C}_{\rm st}$ is described by local energy landscapes with a single minimum at $\mathscr{C}$ and a single maximum at $\mathscr{F}$. Within the bistable engulfment regime $\mathscr{B}_{\rm st}$, the local energy landscapes exhibit two (meta)stable minima at the particle states $\mathscr{F}$ and $\mathscr{C}$ separated by an energy barrier. Finally, within the partial engulfment regime $\mathscr{P}_{\rm st}$, the only extrema of the local energy landscapes are provided by a single minimum corresponding to a partially engulfed state $\mathscr{P}$ and by maxima at the particle states $\mathscr{F}$ and $\mathscr{C}$.

In the preceding discussion, we have implicitly assumed that the energy landscapes do not exhibit any additional minima or maxima. The latter feature is always valid in the small particle limit [134]. In general, one may have additional satellite minima close to the free or completely engulfed states as found by numerical energy minimization for zero spontaneous curvature [140].

8.6 Exocytic Engulfment of Interior Nanoparticles

The (in)stability relations as given by (13)–(16) and the corresponding engulfment regimes described in the previous subsection apply to *endocytic* engulfment of exterior nanoparticles which are dispersed in the exterior aqueous solution and adhere to the outer leaflet of the membranes. The corresponding relations for *exocytic* engulfment of nanoparticles originating from the vesicle interior and adhering to the inner membrane leaflet can be obtained by replacing M, M', and m in (13)–(16) by $-M$, $-M'$, and $-m$, i.e., by changing the sign of all curvatures that appear in these relations. One then finds, in particular, that a membrane segment with $M < -1/R_W$ does not adhere to any particle and that completely engulfed states are impossible for an unbound membrane segment with $M' > 2m + 1/R_W$, irrespective of the size of the particles.

8.7 Engulfment Patterns and Curvature-Induced Forces

The four stability relations (13)–(16) which define the four engulfment regimes depend on the local mean curvatures M and M' of the membrane, with $M = M'$ in the small particle limit. Therefore, when a nonspherical vesicle with variable curvature M is exposed to many nanoparticles, the vesicle membrane can be decomposed, in general, into several membrane segments that belong to different engulfment regimes. As a consequence, nonspherical vesicles exhibit distinct engulfment patterns corresponding to different combinations of the engulfment regimes. However, not all combinations of the four engulfment regimes can be present on a single vesicle but only 10 out of 15 such combinations [132].

When a membrane-bound nanoparticle diffuses within a membrane segment that belongs to the partial engulfment regime $\mathscr{P}_{\mathrm{st}}$, its binding energy depends on the local mean curvature M of the membrane. This M-dependence of the binding energy defines a global energy landscape for the diffusing particle, and the gradient of this global energy landscape provides a curvature-induced force acting on the particle [134]. As a consequence, the nanoparticle undergoes biased diffusion towards membrane segments of lower or higher mean curvature, depending on whether the particle adheres to the outer or inner membrane leaflet, respectively. The partial engulfment of nanoparticles with a chemically uniform surface requires fine-tuning of particle size and adhesiveness with respect to the properties of the membrane. In contrast, Janus particles with one strongly adhesive and one nonadhesive surface domain are always partially engulfed. Therefore, the curvature-induced forces that have been predicted theoretically [134] should be directly accessible to experimental studies when the vesicles are exposed to such Janus particles.

8.8 Further Aspects of Membrane-Nanoparticle Interactions

In the preceding subsections, spherical nanoparticles interacting with uniform membranes have been considered. These membrane–particle systems are governed by the (in)stability conditions (13)–(16) which lead to four engulfment regimes, ten different engulfment patterns, and curvature-induced forces acting on partially engulfed nanoparticles. Generalized (in)stability conditions have also been derived for membranes with two types of intramembrane domains that differ in their fluid-elastic properties [34]. These generalized conditions provide a quantitative description for the nonmonotonic size dependence of clathrin-dependent endocytosis as observed experimentally in [35, 36]. The (in)stability conditions can also be extended to nonspherical particles [133] as studied in [141] by Monte-Carlo simulations. Furthermore, for vanishing spontaneous curvature, another intriguing effect has been observed in simulations: when the membrane–particle adhesion was parametrized in terms of a short-ranged potential well, the nanoparticles were found to assemble into linear aggregates that are enclosed by membrane in-tubes [142–144].

9 Wetting of Membranes by Aqueous Droplets

My renewed interest in spontaneous curvature was triggered by the spontaneous tube formation as observed in aqueous two-phase systems (Fig. 5). I first came across these systems in 2001 when I gave a talk at Penn State and met Christine Keating who was studying lipid vesicles in aqueous PEG-dextran solutions [145]. These solutions can undergo aqueous phase separation and then form PEG-rich and dextran-rich droplets. Such aqueous two-phase systems have been frequently used

in biochemical analysis and biotechnology to separate and purify biomolecules, organelles, and membranes [146]. As explained in the present section, they also provide insight into the wetting behavior of membranes and vesicles, a new research topic which turns out to be rather interesting.

9.1 Transitions Between Distinct Wetting Morphologies

Two experimental methods have been used to induce aqueous phase separation of PEG-dextran solutions within GUVs: temperature changes [145, 147] and osmotic deflation [74, 100, 148, 149]. After the phase separation has been completed, the vesicle contains two aqueous droplets consisting of the PEG-rich phase α and the dextran-rich phase β, which are both separated by the membrane from the exterior phase γ, see insets in Fig. 9. In general, we can distinguish three different wetting morphologies for a membrane in contact with two aqueous phases α and β: the

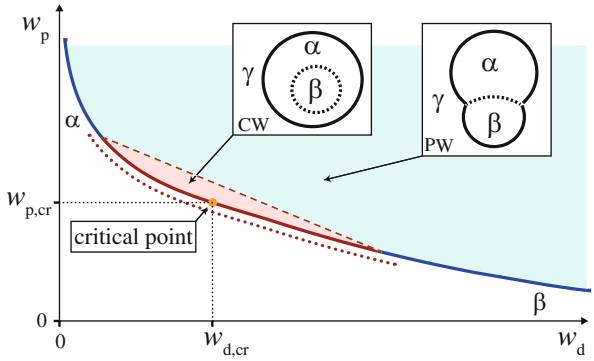

Fig. 9 Phase diagram and membrane wetting behavior of aqueous PEG-dextran solutions as a function of the weight fractions w_p and w_d for the two polymers. The critical demixing point (orange dot) is located at $(w_{d,cr}, w_{p,cr}) = (0.0451, 0.0361)$ [74]. The coexistence region of the PEG-rich phase α and the dextran-rich phase β consists of two subregions, CW (pink) and PW (turquois). In the pink CW subregion close to the critical point, the membrane is completely wetted by the PEG-rich phase α which encloses the dextran-rich phase β, see left inset where γ denotes the exterior phase, and gravitational effects arising from the mass densities of the different phases have been ignored. The CW subregion is separated from the one-phase region (white) by the red segment of the binodal line. In the turquois PW subregion, the membrane is partially wetted by both phases, see right inset. The PW subregion is separated from the one-phase region by the blue segment of the binodal line. The boundary between the CW and PW subregions is provided by a certain tie line (red dashed line), the precise location of which depends on the lipid composition of the membrane. Along this tie line, the system undergoes a complete-to-partial wetting transition. Furthermore, if one approaches the red CW segment of the binodal line from the one-phase region, a wetting layer of the α phase starts to form at the membrane (red dotted line) and becomes mesoscopically thick as one reaches the red CW segment of the binodal line. No such layer is formed along the blue PW segment of the binodal

membrane is wetted (i) completely by the α phase, (ii) completely by the β phase, or (iii) partially by both phases. For the PEG-dextran solutions, both complete wetting by the PEG-rich phase α and partial wetting by both phases have been observed. The corresponding phase diagram is displayed in Fig. 9. As shown in this figure, the two-phase coexistence region of these systems typically consists of two subregions corresponding to complete and partial wetting of the membrane by the PEG-rich phase α. These two subregions are separated by a certain tie line, at which the system undergoes a complete-to-partial wetting transition. The precise location of this tie line depends on the lipid composition of the membranes and has been elucidated for binary lipid mixtures consisting of DOPC and GM1 [100, 148] as well as for ternary mixtures containing DOPC, DPPC, and cholesterol [74]. In general, the wetting transition along this tie line can be continuous or discontinuous depending on the manner in which the contact angle vanishes as we approach the transition from the partial wetting regime. So far, the experimental data do not allow us to draw firm conclusions about the continuous or discontinuous nature of the transition.

A particularly interesting class of aqueous droplets is provided by biomolecular condensates, also known as membraneless organelles, that have been discovered in vivo and are enriched in intrinsically disordered proteins such as FUS [150]. Quite recently, we studied GUVs exposed to such droplets and found that these droplets undergo two distinct wetting transitions: from complete wetting of the membrane by the FUS-poor phase to partial wetting to complete wetting by the FUS-rich phase [151].

9.2 Partial Wetting and Apparent Contact Angles

For partial wetting of a vesicle membrane, both the α and the β droplets are in contact with this membrane (right inset of Fig. 9). As a consequence, the $\alpha\beta$ interface between the two aqueous phases forms a contact line with the membrane that partitions this membrane into two segments, an $\alpha\gamma$ and a $\beta\gamma$ segment, as shown in Fig. 10. Because the two membrane segments are exposed to different aqueous environments, they will in general have different spontaneous curvatures $m_{\alpha\gamma}$ and $m_{\beta\gamma}$ and different bending rigidities $\kappa_{\alpha\gamma}$ and $\kappa_{\beta\gamma}$. Furthermore, the $\alpha\beta$ interface exerts capillary forces onto the vesicle membrane which are counterbalanced by the tensions within the two membrane segments.

The membrane deformations arising from these capillary forces depend on the interfacial tension $\Sigma_{\alpha\beta}$, on the mechanical tensions and fluid-elastic properties of the two membrane segments, as well as on the sizes of the α and β droplets, which are conveniently defined via $(3V_\alpha/4\pi)^{1/3}$ and $(3V_\beta/4\pi)^{1/3}$. So far, the experimental studies have explored the regime in which the α and β droplets were large compared to the length scales $(\kappa_{\alpha\gamma}/\Sigma_{\alpha\beta})^{1/2}$ and $(\kappa_{\beta\gamma}/\Sigma_{\alpha\beta})^{1/2}$. In such a situation, the two membrane segments form two spherical caps which meet the spherical $\alpha\beta$ interface along an apparent contact line as shown in Fig. 10a. This three-spherical-cap geometry is determined by the curvature radii of the three

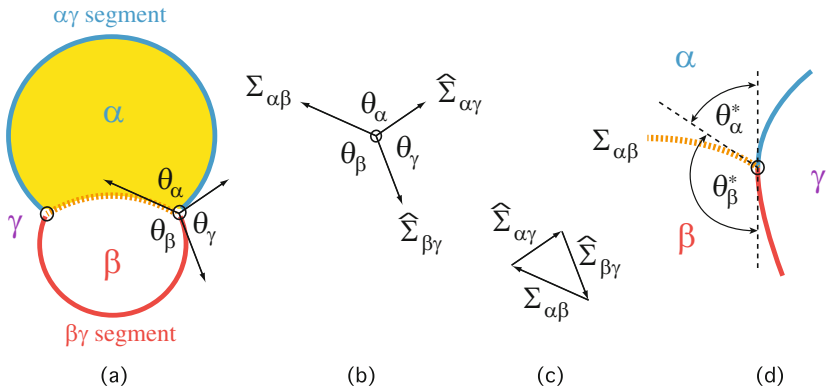

Fig. 10 Vesicle (blue/red) enclosing two aqueous droplets of α and β phase (yellow and white) immersed in the exterior liquid γ corresponding to partial wetting of the membrane by both α and β. The latter two phases are separated by the $\alpha\beta$ interface (broken orange) with interfacial tension $\Sigma_{\alpha\beta}$. This interface partitioned the vesicle membrane into two segments, the $\alpha\gamma$ segment (blue) and the $\beta\gamma$ segment (red). Because the two membrane segments are exposed to two different aqueous environments, they will in general differ in their spontaneous curvatures. (**a**) Vesicle shape consisting of three surface segments that have a spherical shape when viewed with optical resolution. The extrapolation of the spherical membrane segments defines an apparent contact line (black circles) and three apparent contact angles θ_α, θ_β, and θ_γ; [78, 152] (**b**) for certain parameter regimes, see main text, the total membrane tensions $\hat{\Sigma}_{\alpha\gamma}$ and $\hat{\Sigma}_{\beta\gamma}$ balance the interfacial tension $\Sigma_{\alpha\beta}$ along the apparent contact line; (**c**) force balance in (**b**) redrawn as a triangle; and (**d**) enlarged view of the true contact line at which the membrane bends smoothly, and the effective membrane segments have a common tangent plane (vertical broken line). The angles between this common tangent plane and the plane tangential to the $\alpha\beta$ interface represent the intrinsic contact angles θ^*_α and θ^*_β with $\theta^*_\alpha + \theta^*_\beta = \pi$

spherical surface segments and the radius of the apparent contact line [152].[3] Along the contact line, one can measure three apparent contact angles θ_α, θ_β, and θ_γ, see Fig. 10a. Combining the Laplace equation for the $\alpha\beta$ interface with the Euler–Lagrange (or shape) equations for the two membrane segments, one obtains the general relationship [152]

$$M_{\alpha\gamma}\left(\frac{\Sigma^{\rm eff}_{\alpha\gamma}}{\Sigma_{\alpha\beta}} - \frac{\sin\theta_\beta}{\sin\theta_\gamma}\right) = M_{\beta\gamma}\left(\frac{\Sigma^{\rm eff}_{\beta\gamma}}{\Sigma_{\alpha\beta}} - \frac{\sin\theta_\alpha}{\sin\theta_\gamma}\right) \tag{18}$$

[3] In addition, one also has to specify whether the three cap centers are located above or below the plane that contains the contact line.

between the mean curvatures $M_{\alpha\gamma}$ and $M_{\beta\gamma}$ of the two membrane segments, the apparent contact angles $\theta_\alpha, \theta_\beta, \theta_\gamma$ and the effective segment tensions

$$\Sigma_{j\gamma}^{\text{eff}} \equiv \hat{\Sigma}_{j\gamma} - 2\kappa_{j\gamma}\, m_{j\gamma}\, M_{j\gamma} = \Sigma_{j\gamma} + \sigma_{j\gamma} - 2\kappa_{j\gamma}\, m_{j\gamma}\, M_{j\gamma}\,. \tag{19}$$

with $j = \alpha$ or β. The effective tension $\Sigma_{j\gamma}^{\text{eff}}$ consists of the total segment tension $\hat{\Sigma}_{j\gamma} = \Sigma_{j\gamma} + \sigma_{j\gamma}$ and of the curvature-dependent term $2\kappa_{j\gamma}\, m_{j\gamma}\, M_{j\gamma}$. The mechanical segment tensions $\Sigma_{j\gamma}$ can be further decomposed into the overall mechanical stress experienced by the whole membrane, corresponding to the Lagrange multiplier conjugate to the total membrane area, and into the adhesion free energy densities of the two membrane segments [152]. The overall mechanical stress represents a hidden parameter which cannot be measured directly but depends on the vesicle geometry. In order to eliminate this parameter, one may apply the relation (18) to several droplets on the same vesicle.

For certain regions of the parameter space, the force balance along the apparent contact line can be described in a self-consistent manner and then leads to curvature-independent relationships between the apparent contact angles and the total membrane tensions. For each membrane segment $j\gamma$, we can define a regime of small bending energies and a regime of large spontaneous curvatures. Segment $j\gamma$ belongs to the *regime of small bending energy* if the bending energy of this segment is small compared to the interfacial free energy of the $\alpha\beta$ interface. The latter condition is fulfilled if the spontaneous curvature $m_{j\gamma}$ is comparable to or smaller than the mean curvature $M_{j\gamma}$ of the membrane segment and if the water–water interface is large compared to $18\pi\kappa_{j\gamma}/\Sigma_{\alpha\beta}$. On the other hand, segment $j\gamma$ belongs to the *regime of large spontaneous curvature* if the spontaneous curvature $m_{j\gamma}$ is large compared to the mean curvature $M_{j\gamma}$ of this segment. If each membrane segment belongs to the small bending or to the large spontaneous curvature regime, one obtains the force balance conditions [152]

$$\frac{\Sigma_{\alpha\beta}}{\sin\theta_\gamma} = \frac{\hat{\Sigma}_{\alpha\gamma}}{\sin\theta_\beta} = \frac{\hat{\Sigma}_{\beta\gamma}}{\sin\theta_\alpha} \tag{20}$$

along the apparent contact line which relate the total membrane tensions $\hat{\Sigma}_{\alpha\gamma}$ and $\hat{\Sigma}_{\beta\gamma}$ of the two membrane segments to the apparent contact angles and the interfacial tension $\Sigma_{\alpha\beta}$. The conditions in (20) are equivalent to the tension ratios

$$\frac{\hat{\Sigma}_{\alpha\gamma}}{\Sigma_{\alpha\beta}} = \frac{\sin\theta_\beta}{\sin\theta_\gamma} \quad \text{and} \quad \frac{\hat{\Sigma}_{\beta\gamma}}{\Sigma_{\alpha\beta}} = \frac{\sin\theta_\alpha}{\sin\theta_\gamma}\,. \tag{21}$$

as used in [48, 78]. These equations represent the law of sines for a triangle with the three sides $\Sigma_{\alpha\beta}$, $\hat{\Sigma}_{\alpha\gamma}$, and $\hat{\Sigma}_{\beta\gamma}$ as displayed in Fig. 10b, c. Therefore, in the parameter regimes of small bending energies and/or large spontaneous curvatures, the total membrane tensions can be deduced from the measured values of the apparent contact angles and of the interfacial tension $\Sigma_{\alpha\beta}$.

If one membrane segment, say the $\alpha\gamma$ segment, forms nanotubes, the mean curvature $M_{\alpha\gamma}$ of the $\alpha\gamma$-segment is much smaller than the mean curvature of the tubes which is of the order of the spontaneous curvature $m_{\alpha\gamma}$. In such a situation, the mechanical tension $\Sigma_{\alpha\gamma}$ turns out to be much smaller than the spontaneous tension $\sigma_{\alpha\gamma}$ [78] and the total membrane tension $\hat{\Sigma}_{\alpha\gamma} \approx \sigma_{\alpha\gamma} = 2\kappa_{\alpha\gamma}\, m_{\alpha\gamma}^2$. When we combine this asymptotic equality with the first relationship in (21), we obtain the spontaneous curvature

$$m_{\alpha\gamma} = -\left(\frac{\Sigma_{\alpha\beta}}{2\kappa_{\alpha\gamma}}\,\frac{\sin(\theta_\beta)}{\sin(\theta_\gamma)}\right)^{1/2} \tag{22}$$

where the minus sign reflects the experimental observation that the nanotubes protrude into the interior compartment of the vesicle as in Fig. 5. The $m_{\alpha\gamma}$-values obtained from (22) have been confirmed in [74] by two other, completely independent methods to deduce the spontaneous curvature.

9.3 Intrinsic Contact Angles

If the spherical cap geometry shown in Fig. 10a persisted to nanoscopic scales, the vesicle membrane would have a kink along the true contact line. Such a kink would lead to an infinite bending energy of the membrane. Therefore, along the true contact line, the membrane should be smoothly curved and the geometry is then characterized by intrinsic contact angles [149, 152]. As shown in Fig. 10d, the common tangent plane to the two membrane segments along the true contact line defines two intrinsic angles θ_α^* and θ_β^* which are related via $\theta_\alpha^* + \theta_\beta^* = \pi$.

The total (free) energy of the system consists of the bending energy of the membrane, the interfacial free energy of the water–water interface, and the line energy of the three-phase contact line. The latter contribution is proportional to the line tension $\lambda_{\rm co}$ of the contact line. Minimizing this free energy for axisymmetric morphologies, one obtains the balance condition [152]

$$\Sigma_{\beta\gamma} - \Sigma_{\alpha\gamma} = \Sigma_{\alpha\beta}\cos\theta_\alpha^* + \lambda_{\rm co}\,\frac{\cos\psi_{\rm co}}{R_{\rm co}} + \Delta_{\Sigma,{\rm co}} \tag{23}$$

between the mechanical segment tensions $\Sigma_{\beta\gamma}$ and $\Sigma_{\alpha\gamma}$, the interfacial tension $\Sigma_{\alpha\beta}$, and the line tension $\lambda_{\rm co}$. The parameter $R_{\rm co}$ is the radius of the true contact line, and $\psi_{\rm co}$ is the tilt angle between the symmetry axis and the common tangent plane of the two membrane segment at the true contact line. The additional term $\Delta_{\Sigma,{\rm co}}$ depends on the local curvatures of the two membrane segments along this contact line, compare Fig. 10d, and vanishes if the two membrane segments have the same curvature-elastic properties [152]. In the latter case, the balance condition (23) along

the true contact line simplifies and becomes

$$\Sigma_{\beta\gamma} - \Sigma_{\alpha\gamma} = \hat{\Sigma}_{\beta\gamma} - \hat{\Sigma}_{\alpha\gamma} = \Sigma_{\alpha\beta} \cos\theta_\alpha^* + \lambda_{\rm co} \frac{\cos\psi_{\rm co}}{R_{\rm co}} \,. \tag{24}$$

If both segments belong to the small bending energy regime or to the large spontaneous curvature regime, we can combine the balance condition (24) with the tension ratios in (21) which then describes the force balance along the apparent contact line. As a result, we obtain the simple relation

$$\cos\theta_\alpha^* = \frac{\sin\theta_\alpha - \sin\theta_\beta}{\sin\theta_\gamma} - \frac{\lambda_{\rm co}}{\Sigma_{\alpha\beta}} \frac{\cos\psi_{\rm co}}{R_{\rm co}} \tag{25}$$

between the intrinsic contact angle θ_α^* that is not accessible to conventional optical microscopy and the apparent contact angles that can be obtained from the microscopy images.

In [149], the relation (25) was originally derived for the special case of vanishing spontaneous curvatures for both membrane segments, i.e., $m_{\alpha\gamma} = m_{\beta\gamma} = 0$, and was then used to analyze the shapes of vesicles that enclosed one PEG-rich and one dextran-rich droplet. Even though the apparent contact angles of these vesicles were quite different, the relation (25) led to a fairly constant value for the intrinsic contact angle θ_α^*. Later experiments revealed, however, that the spontaneous curvatures $m_{\alpha\gamma}$ must be quite large because the $\alpha\gamma$ membrane segments in contact with the PEG-rich phase formed nanotubes with a suboptical width as in Fig. 5 [74, 100]. Furthermore, the experimental data as well as molecular dynamics simulations provided strong evidence that this large spontaneous curvature was generated by asymmetric adsorption of PEG molecules. Therefore, it is tempting to assume that the spontaneous curvature $m_{\beta\gamma}$ of the $\beta\gamma$ membrane segments in contact with the dextran-rich phase was comparatively small. A small value of $m_{\beta\gamma}$ and a large value of $m_{\alpha\gamma}$ would justify the use of (21) to describe the force balance along the apparent contact line but it would not justify the use of (24) to describe the force balance along the true contact line because (24) is based on the assumption that both membrane segments have essentially the same spontaneous curvature. On the other hand, if we assumed that the spontaneous curvature $m_{\beta\gamma}$ is large as well and comparable to $m_{\alpha\gamma}$, we could justify the use of both relations (21) and (24).

9.4 Nucleation and Growth of Nanodroplets at Membranes

For complete wetting of the vesicle membrane by the α phase, the intrinsic contact angle θ_α^* vanishes which implies that the phase separation starts via the formation of a thin α layer at the vesicle membrane (broken red line in Fig. 9). For partial wetting, on the other hand, the intrinsic contact angle $\theta_\alpha^* > 0$, and the phase separation starts with the nucleation of α droplets at the membrane surface as shown in Fig. 11a,

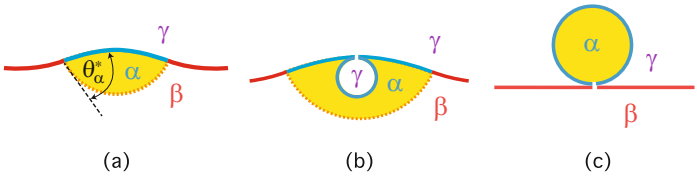

Fig. 11 Nucleation and growth of an α droplet (yellow) that is formed at a vesicle membrane (blue/red). As in Fig. 10, the two aqueous phases α and β are in contact with the inner membrane leaflet, and γ denotes the exterior aqueous phase: (**a**) The $\alpha\beta$ interface (broken orange) between the α droplet and the other interior phase β has the shape of a spherical cap and forms the intrinsic contact angle θ_α^* with the adjacent $\alpha\gamma$ segment (blue) of the membrane. Because the latter segment is now exposed to an asymmetric environment, it can acquire an appreciable spontaneous curvature $m_{\alpha\gamma}$. Of particular interest is the case for which the curvature $m_{\alpha\gamma}$ is large compared to the spontaneous curvature $m_{\beta\gamma}$ of the $\beta\gamma$ membrane segment (red); (**b**) for negative values of $m_{\alpha\gamma}$, the $\alpha\gamma$ membrane segment prefers to form a spherical in-bud that is filled with exterior γ phase; and (**c**) for positive values of $m_{\alpha\gamma}$, the $\alpha\gamma$ membrane segment prefers to engulf the α droplet provided that the volume of the droplet matches the preferred bud size. Complete engulfment leads to a closed membrane neck that replaces the $\alpha\beta$ interface, thereby eliminating the contribution of this interface to the system's free energy

corresponding to a critical nucleus with a radius of tens of nanometers. For such a small droplet, the intrinsic contact angle will be affected by the line tension λ_{co} of the contact line. The line tension can be positive or negative, in contrast to the line tension λ of domain boundaries which is always positive. In fact, recent molecular simulations indicate that the contact line tension λ_{co} is typically negative [153].

After an α droplet as in Fig. 11a has been formed, the $\alpha\gamma$ segment of the membrane, which is in contact with this droplet, is exposed to an asymmetric environment and can acquire an appreciable spontaneous curvature $m_{\alpha\gamma}$. In order to simplify the following discussion, let us assume that the curvature $m_{\alpha\gamma}$ is large compared to the spontaneous curvature $m_{\beta\gamma}$ of the $\beta\gamma$ segment and that the latter curvature is small and can be ignored.

If the spontaneous curvature $m_{\alpha\gamma}$ is *negative* as in the case of PEG-dextran solutions that undergo aqueous phase separation within the vesicles, the membrane prefers to curve towards the inner leaflet and to form a spherical in-bud of radius $R_\gamma \simeq 1/(2|m_{\alpha\gamma}|)$ that is filled with the exterior γ phase as in Fig. 11b. Such an in-bud represents a limit shape with a closed neck that can be characterized by the condition [78, 91] $M_a + M_b = 2m_{\alpha\gamma}$ where $M_a = -1/R_\gamma$ and M_b are the mean curvatures of the two membrane segments a and b adjacent to the neck. The in-bud displaces some volume of α phase and *increases* the area of the $\alpha\beta$ interface which implies that the α droplet has to reach a volume large compared to $4\pi R_\gamma^3/3$ before the in-bud becomes energetically favorable. After such an in-bud has formed, the bud radius increases until the spherical shape becomes unstable and transforms into a short necklace-like tube [74, 101].

On the other hand, if the droplet-induced curvature $m_{\alpha\gamma}$ is *positive*, the $\alpha\gamma$ membrane segment prefers to curve towards the outer leaflet of the vesicle membrane and to form a spherical out-bud of radius $R_\alpha \simeq 1/m_{\alpha\gamma}$ that is filled with α phase as in

Fig. 11c. Such an out-bud with a closed membrane neck reduces the free energy of the membrane-droplet system by (i) adapting the mean curvature of the $\alpha\gamma$ segment to its spontaneous curvature $m_{\alpha\gamma}$ and (ii) replacing the $\alpha\beta$ interface by a closed membrane neck which implies a strong reduction of the interfacial free energy. Spherical buds with closed necks are also formed during domain-induced budding in the absence of aqueous phase separation [3, 5]. Compared to domain-induced budding, the closed neck in Fig. 11c is further stabilized by the formation of an $\alpha\beta$ interface during neck opening. For an axisymmetric neck, the area of this interface depends quadratically on the neck radius $R_{\rm ne}$ which implies a free energy increase proportional to $\Sigma_{\alpha\beta} R_{\rm ne}^2$ and the same closed neck condition as for domain-induced buds [152]. However, recent simulations revealed that negative line tensions break the axisymmetry and lead to tight-lipped membrane necks [153].

Even in the absence of budding, the existence of a complete-to-partial wetting transition implies some interesting behavior of the aqueous droplets. Thus, consider again a droplet as in Fig. 11a and assume that we now change the conditions from partial to complete wetting. The localized droplet will then be transformed into a delocalized film that covers the whole membrane, and this morphological transformation can be used to redistribute molecules within the aqueous subcompartment.

10 Topological Transformations of Membranes

In the previous sections, I focused on processes that do not change the topology of the membranes. Now, let us briefly consider two important topology-transforming processes, membrane fusion and membrane fission (or scission). During membrane fusion, two separate membranes are combined into a single one; during fission, a single membrane is divided up into two separate ones. These processes are ubiquitous in eukaryotic cells: Both the outer cell membrane and the inner membranes of organelles act (i) as donor membranes that continuously produce vesicles via budding and fission and (ii) as acceptor membranes that integrate such vesicles via adhesion and fusion. One example for fission is provided by the closure of autophagosomes which are double-membrane organelles [154, 155].

10.1 Free Energy Landscapes of Fusion and Fission

It is instructive to consider the free energy landscapes for fusion and fission as schematically depicted in Fig. 12. Fusion is exergonic, if the free energy G_2 of the 2-vesicle state exceeds the free energy G_1 of the 1-vesicle state. In the opposite case with $G_1 > G_2$, fission is exergonic. Exergonic fusion or fission processes occur spontaneously but the kinetics of these processes is governed by the free energy barriers Δ between the 1-vesicle and the 2-vesicle state, see Fig. 12. Because these barriers are typically large compared to $k_{\rm B}T$, even exergonic fusion and fission

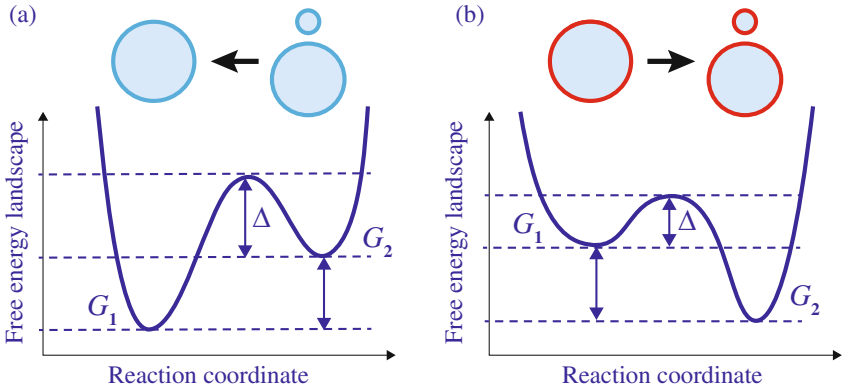

Fig. 12 Free energy landscapes for membrane fusion and fission (or scission): (**a**) schematic landscape for an exergonic fusion process. In this case, the free energy G_2 of the 2-vesicle state exceeds the free energy G_1 of the 1-vesicle state; and (**b**) schematic landscape for an exergonic fission process. In the latter case, the free energy G_1 of the 1-vesicle state is larger than the free energy G_2 of the 2-vesicle state. The cartoons (top row) show a 1-vesicle state on the left and a 2-vesicle state on the right; both states have the same membrane area. The small vesicle of the 2-vesicle state has the radius R_{ss} which is much smaller than the radius of the large vesicle. The dark blue membranes in (**a**) have a spontaneous curvature with magnitude $|m| \ll 1/R_{ss}$ whereas the red membranes in (**b**) have a large spontaneous curvature with $m \simeq 1/(2R_{ss})$. In both (**a**) and (**b**), the free energy difference $G_2 - G_1$ determines the direction in which the processes can proceed spontaneously (black arrows), while the kinetics of these processes is governed by the free energy barriers Δ

processes will be rather slow unless coupled to other molecular processes that act to reduce these barriers. Indeed, in the living cell, the fusion and fission of biomembranes is controlled by membrane-bound proteins such as SNAREs and dynamin as will be discussed in later chapters of this book. It should also be emphasized that the free energy landscape may involve several barriers as has been observed in molecular dynamics simulations of tension-induced fusion [67, 69].

The free energy difference $G_2 - G_1$ between the 2-vesicle and the 1-vesicle state can be estimated by the corresponding changes in curvature energy [156]. Because of the topological changes, we need to take the Gaussian curvature and the associated Gaussian curvature modulus κ_G into account [90]. Stability arguments indicate that $-2 < \kappa_G/\kappa < 0$ [157]. For the following considerations, it will be sufficient to use the rough estimate $\kappa_G \simeq -\kappa$ which is consistent with both experimental [158, 159] and simulation [62] studies. A small spherical vesicle that is cleaved off from a donor membrane then changes the total curvature energy by a certain amount that can be used to estimate the free energy difference $G_2 - G_1$. It is important to realize, however, that this change in curvature energy depends strongly on the magnitude of the spontaneous curvature as shown in the next subsections.

10.2 Exergonic Fusion for Small Spontaneous Curvatures

Let us consider a 1-vesicle state corresponding to a spherical GUV that acts as the donor membrane and a 2-vesicle state obtained from this GUV by cleaving off a much smaller spherical vesicle, see top row of Fig. 12. Both states have the same membrane area. The small vesicle of the 2-vesicle state has the radius $R_{\rm ss}$ which is taken to be much smaller than the radius of the GUV. We may then ignore any constraints on the vesicle volumes and assume that the large vesicle of the 2-vesicle state has a spherical shape as well. If the GUV membrane is uniform, and the magnitude $|m|$ of its spontaneous curvature is much smaller than the inverse size, $1/R_{\rm ss}$, of the small vesicle, the free energy difference between the 2-vesicle and 1-vesicle state is *positive* and has the form

$$G_2 - G_1 = 8\pi\kappa + 4\pi\kappa_G \simeq +4\pi\kappa \quad \text{for } |m| \ll 1/R_{\rm ss} \tag{26}$$

where the estimate $\kappa_G \simeq -\kappa$ has been used. In this case, the fission process is endergonic whereas the fusion process is exergonic, see the corresponding free energy landscape in Fig. 12a. For the typical rigidity value $\kappa \simeq 20\, k_{\rm B}T$, the relation (26) leads to the large free energy difference $G_2 - G_1 \simeq +250\, k_{\rm B}T$!

10.3 Exergonic Fission for Large Spontaneous Curvatures

On the other hand, if the magnitude $|m|$ of the spontaneous curvature is large, the GUV can form a small spherical bud with radius $R_{\rm ss} \simeq 1/(2|m|)$ as in Fig. 12b as follows from the closed neck condition for the corresponding limit shape.[4] If this bud is cleaved off, the free energy difference between the resulting 2-vesicle state and the initial 1-vesicle state is now *negative* and given by

$$G_2 - G_1 = 8\pi\kappa(1 - 2R_{\rm ss}|m|) + 4\pi\kappa_G \simeq 4\pi\kappa_G \simeq -4\pi\kappa \quad \text{for } R_{\rm ss} \simeq 1/(2|m|). \tag{27}$$

In the latter case, the fission process is exergonic and the fusion process is endergonic, corresponding to a free energy landscape as in Fig. 12b. Now, the free energy difference $G_2 - G_1 \simeq -250\, k_{\rm B}T$ for the typical value $\kappa \simeq 20\, k_{\rm B}T$ of the bending rigidity.

[4] For $m > 0$ and $m < 0$, this limit shape involves a spherical out- and in-bud, respectively, corresponding to the shapes $L^{\rm pear}$ and $L^{\rm sto}$ in [91].

10.4 Free Energy Difference for Domain-Induced Fission

Biological membranes often form intramembrane domains with an appreciable spontaneous curvature $m_{\rm do}$. One example for this latter case is provided by clathrin-dependent endocytosis which leads to membrane domains with a spontaneous curvature $m_{\rm do} \simeq -1/(40\,{\rm nm})$ [34]. Now, consider a GUV with a small membrane domain with an appreciable spontaneous curvature $m_{\rm do}$ whereas the spontaneous curvature of the remaining GUV membrane is again negligible. The membrane domain can then form a small spherical bud of size $R_{\rm ss} = 1/|m_{\rm do}|$ as follows from the closed neck condition for domain-induced budding [5]. If the latter bud is cleaved off, the free energy difference between the resulting 2-vesicle state and the initial 1-vesicle state is again negative and now has the form

$$G_2 - G_1 = 8\pi\kappa(1-2R_{\rm ss}|m_{\rm do}|) + 4\pi\kappa_G - 4\pi\frac{\lambda}{|m_{\rm do}|} \simeq -12\pi\kappa - 4\pi\frac{\lambda}{|m_{\rm do}|} \qquad (28)$$

where λ denotes the line tension of the domain boundary. Because this line tension has to be positive, the fission of a domain-induced bud is an exergonic process that leads to an even larger free energy gain $|G_2 - G_1| > 12\pi\kappa \gtrsim 750\,k_{\rm B}T$ for bending rigidity $\kappa \simeq 20\,k_{\rm B}T$.

11 Summary and Outlook

During the last 20 years, we have seen a fair number of rather interesting developments related to the biophysics of membranes and vesicles. One important development was the identification of several lipid mixtures that can separate into two fluid phases. This development was triggered by the proposal that cellular membranes contain lipid rafts enriched in sphingomyelin and cholesterol [8]. So far, we do not have any images of such phase domains in vivo. On the other hand, cell membranes are expected to be partitioned into many distinct membrane segments that are exposed to different molecular environments. Long-lived components of these heterogeneous environments arise from the cytoskeletal cortex as revealed by single particle tracking of membrane-bound nanoparticles [42]. If lipid phase domains form in such a cell membrane, the domain formation is necessarily restricted to one of the membrane segments and, thus, hard to detect [48]. In the limiting case in which the environmental heterogeneities of the cell membrane act as long-lived random fields, membrane phase separation would be completely destroyed.

Another development that had a large impact on the field was the identification of proteins that generate local membrane curvature. These proteins can be viewed as Janus particles with strongly nonspherical shapes (Fig. 4). It should be rather interesting to synthesize such Janus particles and to study their interactions with

lipid membranes. In the last couple of years, reliable methods have been developed to determine the spontaneous curvature of membranes from their spontaneous [74, 100] or force-induced [117] tubulation. Using the relation (1), we can then deduce the locally generated curvature of single membrane-bound "particles" from the coverages on the two leaflets of the membranes [85, 86]. Furthermore, because the nanotubes provide a reservoir for membrane area, the mother vesicles of tubulated vesicles exhibit an increased robustness against mechanical perturbations as recently demonstrated by micropipette aspiration [101].

Membrane nanotubes are also formed within eukaryotic cells and provide ubiquitous structural elements of many membrane-bound organelles such as the endoplasmic reticulum, the Golgi, the endosomal network, and mitochondria [160–162]. These intracellular nanotubes are used for molecular sorting, signalling, and transport. Intercellular (or "tunneling") nanotubes formed by the plasma membranes of two or more cells provide long-distance connections for cell–cell communication, intercellular transport, and virus infections [163–165]. It seems rather plausible to assume that these tubes are also generated by spontaneous curvature and/or locally applied forces but the relative importance of these two tubulation mechanisms remains to be elucidated for cellular membranes.

As far as the engulfment of nanoparticles by membranes is concerned, we now have a rather detailed theory which leads to the stability conditions (13)–(16) and predicts several critical particle sizes for the engulfment process [34], complex engulfment patterns on GUVs [132], and curvature-induced forces leading to biased diffusion of partially engulfed particles [134]. The theory has been extended to the engulfment by membrane domains [34] and can then explain the nonmonotonic size dependence of clathrin-dependent endocytosis as observed for the uptake of gold particles by HeLa cells [35, 36]. In addition, the stability conditions for closed membrane necks have been generalized to include constriction forces, see the closed neck condition (17), and applied to a variety of membrane systems such as giant plasma membrane vesicles formed by eukaryotic cells and outer membrane vesicles secreted by bacteria [133]. I am rather curious to see experimental studies that scrutinize these predictions.

Another fairly interesting topic that has been hardly explored at all is the wetting behavior of membranes and vesicles in contact with several aqueous phases. So far, this behavior has only been studied for three lipid compositions exposed to aqueous solutions of PEG and dextran [74, 100, 148] as well as to aqueous droplets or membraneless organelles enriched in the intrinsically disordered FUS protein [151] but, quite unexpectedly, all of these systems were found to exhibit wetting transitions (Fig. 9). Another aspect of wetting that remains to be elucidated in a systematic manner, both theoretically and experimentally, is the nucleation and growth of nanodroplets at membranes (Fig. 11).

In the context of synthetic biology, GUVs have long been discussed as possible micro-compartments for the bottom-up assembly of artificial protocells. One practical problem that has impeded research in this direction is the limited robustness of GUVs against mechanical perturbations. Very recently, this limitation has been overcome by two different strategies. One strategy is based on the formation of

GUVs within microfluidic emulsion droplets that support and stabilize the GUVs [166]. The other strategy uses the special properties of tubulated GUVs which can respond to external perturbations by exchanging membrane area between the nanotubes and the mother vesicles [101]. Compared to conventional GUVs, both droplet-stabilized and tubulated GUVs are much more robust against mechanical forces and thus provide new modules for the bottom-up assembly of artificial cells.

Acknowledgements I thank all my coworkers for enjoyable collaborations and Jaime Agudo-Canalejo for a critical reading of the manuscript.

References

1. Lipowsky R, Sackmann E (eds) (1995) Handbook of biological physics, vol 1. Elsevier, Amsterdam
2. Lipowsky R (2019) In: Dimova R, Marques C (eds) The giant vesicle book. Taylor & Francis
3. Lipowsky R (1992) J Phys II France 2:1825
4. Lipowsky R (1993) Biophys J 64:1133
5. Jülicher F, Lipowsky R (1993) Phys Rev Lett 70:2964
6. Baumgart T, Hess S, Webb W (2003) Nature 425:821
7. Riske KA, Bezlyepkina N, Lipowsky R, Dimova R (2006) Biophys Rev Lett 1:387
8. Simons K, Ikonen E (1997) Nature 387:569
9. Korlach J, Schwille P, Webb W, Feigenson G (1999) Proc Natl Acad Sci USA 96:8461
10. Dietrich C, Bagatolli L, Volovyk Z, Thompson N, Levi M, Jacobson K, Gratton E (2001) Biophys J 80:1417
11. Veatch S, Keller S (2003) Biophys J 85:3074
12. Jülicher F, Lipowsky R (1996) Phys Rev E 53:2670
13. Kumar S, Gompper G, Lipowsky R (2001) Phys Rev Lett 86:3911
14. Baumgart T, Das S, Webb WW, Jenkins JT (2005) Biophys J 89:1067
15. Semrau S, Idema T, Holtzer L, Schmidt T, Storm C (2008) Phys Rev Lett 100:088101
16. Bacia K, Schwille P, Kurzchalia T (2005) Proc Natl Acad Sci USA 102:3272
17. Dimova R, Riske KA, Aranda S, Bezlyepkina N, Knorr RL, Lipowsky R (2007) Soft Matter 3:817
18. Jensen MH, Morris EJ, Simonsen AC (2007) Langmuir 23:8135
19. Garg S, Rühe J, Lüdtke K, Jordan R, Naumann CA (2007) Biophys J 92:1263
20. Kiessling V, Wan C, Tamm LK (2009) Biochim Biophys Acta 1788:64
21. Collins MD, Keller SL (2008) Proc Natl Acad Sci USA 105(1):124
22. Orth A, Johannes L, Römer W, Steinem C (2012) Chem Phys Chem 13:108
23. David JH, Clair JJ, Juhasz J (2009) Biophys J 96:521
24. Veatch SL, Gawrisch K, Keller SL (2006) Biophys J 90:4428
25. Vequi-Suplicy C, Riske K, Knorr R, Dimova R (2010) Biochim Biophys Acta 1798:1338
26. Uppamoochikkal P, Tristram-Nagle S, Nagle JF (2010) Langmuir 26(22):17363
27. Pataraia S, Liu Y, Lipowsky R, Dimova R (2014) Biochim Biophys Acta 1838:2036
28. Baumgart T, Hammond AT, Sengupta P, Hess ST, Holowka DA, Baird BA, Webb WW (2007) Proc Natl Acad Sci USA 104:3165
29. Veatch SL, Cicuta P, Sengupta P, Honerkamp-Smith A, Holowka D, Baird B (2008) ACS Chem Biol 3:287
30. Owen DM, Williamson DJ, Magenau A, Gaus K (2012) Nat Commun 3:1256
31. Eggeling C, Ringemann C, Medda R, Schwarzmann G, Sandhoff K, Polyakova S, Belov VN, Hein B, von Middendorff C, Schönle A, Hell SW (2009) Nature 457:1159

32. Mueller V, Ringemann, C, Honigmann A, Schwarzmann G, Medda R, Leutenegger M, Polyakova S, Belov VN, Hell SW, Eggeling C (2011) Biophys J 101:1651
33. Klotzsch E, Schütz GJ (2013) Philos Trans R Soc B 368:20120033
34. Agudo-Canalejo J, Lipowsky R (2015) ACS Nano 9:3704
35. Chithrani BD, Ghazani AA, Chan WCW (2006) Nano Lett 6(4):662
36. Chithrani BD, Chan WCW (2007) Nano Lett 7(6):1542
37. Pezeshkian W, Gao H, Arumugam S, Becken U, Bassereau P, Florent JC, Ipsen JH, Johannes L, Shillcock JC (2016) ACS Nano 11:314
38. Avalos-Padilla Y, Knorr RL, ~~Lipowsky R, Dimova R~~ (2018) Front Cell Infect Microbiol 8:53. https://doi.org/10.3389/fcimb.2018.00053
39. Sako Y, Kusumi A (1994) J Cell Biol 125(6):1251
40. Saxton MJ, Jacobson K (1997) Annu Rev Biophys Biomol Struct 26:373–399
41. Fujiwara T, Ritchie K, Murakoshi H, Jacobson K, Kusumi A (2002) J Cell Biol 157(6):1071
42. Kusumi A, Nakada C, Ritchie K, Murase K, Suzuki K, Murakoshi H, Kasai RS, Kondo J, Fujiwara T (2005) Annu Rev Biophys Biomol Struct 34:351
43. Andrews NL, Lidke KA, Pfeiffer JR, Burns AR, Wilson BS, Oliver JM, Lidke DS (2008) Natl Cell Biol 10(8):955
44. Treanor B, Depoil D, Gonzalez-Granja A, Barral P, Weber M, Dushek O, Bruckbauer A, Batista FD (2010) Immunity 32:187
45. Jaqaman K, Kuwata H, Touret N, Collins R, Trimble WS, Danuser G, Grinstein S (2011) Cell 146:593
46. Rouhiparkouhi T, Weikl TR, Discher DE, Lipowsky R (2013) Int J Mol Sci 14:2203
47. Lipowsky R, Rouhiparkouhi T, Discher DE, Weikl TR (2013) Soft Matter 9:8438
48. Lipowsky R (2014) Biol Chem 395:253
49. Skau CT, Kovar DR (2010) Curr Biol 20:1415
50. Michelot A, Drubin DG (2011) Curr Biol 21:R560
51. Loerke D, Mettlen M, Yarar D, Jaqaman K, Jaqaman H, Danuser G, Schmid SL (2009) PLOS Biol 7(3):e1000057
52. Cureton DK, Harbison CE, Parrish CR, Kirchhausen T (2012) J Virol 86(9):5330
53. Binder K (1983) Z Phys B 50:343
54. Aizenman M, Wehr J (1989) Phys Rev Lett 62:2503
55. Fischer T, Vink RLC (2011) J Chem Phys 134:055106
56. Goetz R, Gompper G, Lipowsky R (1999) Phys Rev Lett 82:221
57. Goetz R, Lipowsky R (1998) J Chem Phys 108:7397
58. Brandt EG, Braun AR, Sachs JN, Nagle JF, Edholm O (2011) Biophys J 100:2104
59. Watson MC, Penev ES, Welch PM, Brown FLH (2011) J Chem Phys 135:244701
60. Tarazona P, Chacon E, Bresme F (2013) J Chem Phys 139:094902
61. Orsi M, Haubertin DY, Sanderson WE, Essex JW (2008) J Phys Chem B 112:802
62. Hu M, Briguglio JJ, Deserno M (2012) Biophys J 102(6):1403
63. Rózycki B, Lipowsky R (2015) J Chem Phys 142:054101
64. Rózycki B, Lipowsky R (2016) J Chem Phys 145:074117
65. Lipowsky R, Döbereiner HG (1998) Europhys Lett 43:219
66. Shillcock J, Lipowsky R (2005) Nat Mater 4:225
67. Grafmüller A, Shillcock J, Lipowsky R (2007) Phys Rev Lett 98:218101
68. Gao L, Lipowsky R, Shillcock JC (2008) Soft Matter 4:1208
69. Grafmüller A, Shillcock JC, Lipowsky R (2009) Biophys J 96:2658
70. Smirnova Y, Marrink S, Lipowsky R, Knecht V (2010) J Am Chem Soc 132:6710
71. Hu J, Lipowsky R, Weikl TR (2013) Proc Natl Acad Sci USA 110:15283
72. Xu GK, Hu J Lipowsky R, Weikl TR (2015) J Chem Phys 143:243136
73. Hu J, Xu GK, Lipowsky R, Weikl TR (2015) J Chem Phys 143:243137
74. Liu Y, Agudo-Canalejo J, Grafmüller A, Dimova R, Lipowsky R (2016) ACS Nano 10:463
75. Lipowsky R (1995) Europhys Lett 30:197
76. Nikolov V, Lipowsky R, Dimova R (2007) Biophys J 92:4356
77. Deserno M (2004) Phys Rev E 69:031903

78. Lipowsky R (2013) Faraday Discuss 161:305
79. Peter BJ, Kent HM, Mills IG, Vallis Y, Butler PJG, Evans PR, McMahon HT (2004) Science 303:495
80. Simunovic M, Yee C. K, Lee, Bassereau P (2015) Soft Matter 11:5030
81. Graber ZT, Shi Z, Baumgart T (2017) Phys Chem Chem Phys 19:15285
82. Farsad K, Ringstad N, Takei K, Floyd SR, Rose K, Camilli PD (2001) J Cell Biol 155(2):193
83. Wang Q, Navarro VAS, Peng G, Molinelli E, Goh SL, Judson BL, Rajashankar KR, Sondermann H (2009) Proc Natl Acad Sci USA 106(31):12700
84. Ford MG, Mills IG, Peter BJ, Vallis Y, Praefcke GJ, Evans PR, McMahon HT (2002) Nature 419:361
85. Breidenich M, Netz R, Lipowsky R Europhys Lett (2000) 49:431
86. Lipowsky R (2002) J Biol Phys 28:195
87. Bancroft WD (1913) J Phys Chem 17:501
88. Bancroft W, Tucker C (1927) J Phys Chem 31:1681
89. Frank FC (1958) Discuss Faraday Soc 25:19
90. Helfrich W (1973) Z Naturforsch 28C:693
91. Seifert U, Berndl K, Lipowsky R (1991) Phys Rev A 44:1182
92. Evans E (1974) Biophys J 14:923
93. Svetina S, Zeks B (1989) Eur Biophys J 17:101
94. Miao L, Seifert U, Wortis M, Döbereiner HG (1994) Phys Rev E 49:5389
95. Döbereiner HG, Evans E, Kraus M, Seifert U, Wortis M (1997) Phys Rev E 55(4):4458
96. Lipowsky R (1999) In: Reguera D, Rubi JM, Vilar JMB (eds) Statistical mechanics of biocomplexity. Lecture notes in physics. Springer, Berlin, pp 1–23
97. Bruckner RJ, Mansy SS, Ricardo A, Mahadevan L, Szostak JW (2009) Biophys J 97:3113
98. Domanov YA, Kinnunen PKJ (2006) Biophys J 91:4427
99. Arouni A, Kiessling V, Tamm L, Dathe M, Blume A (2011) J Phys Chem 115:158
100. Li Y, Lipowsky R, Dimova R (2011) Proc Natl Acad Sci USA 108:4731
101. Bhatia T, Agudo-Canalejo J, Dimova R, Lipowsky R (2018) ACS Nano 12:4478
102. Hochmuth R, Mohandas N, Blackshear PL Jr (1973) Biophys J 13:747
103. Schmidtke DW, Diamond SL (2000) J Cell Biol 149:719
104. Dopheide SM, Maxwell JJ, Jackson SP (2002) Blood 99:159
105. Hochmuth RM, Wiles HC, Evans EA, McCown JT (1982) Biophys J 39:83
106. Brochard-Wyart F, Borghi N, Cuvelier D, Nassoy P (2006) Proc Natl Acad Sci USA 103:7660
107. Waugh RE Biophys J 38:29 (1982)
108. Dasgupta R, Dimova R (2014) J Phys D Appl Phys 47:282001
109. Borghi N, Rossier O, Brochard-Wyart F (2003) Europhys Lett 64:837
110. Tian A, Capraro BR, Esposito C, Baumgart T (2009) Biophys J 97:1636
111. Zhu C, Das SL, Baumgart T (2012) Biophys J 102:1837
112. Bo L, Waugh RE (1989) Biophys J 55:509
113. Ashkin A, Dziedzic JM (1989) Proc Natl Acad Sci USA 86:7914
114. Dai J, Sheetz MP (1995) Biophys J 68:988
115. Hochmuth RM, Shao JY, Dai J, Sheetz MP (1996) Biophys J 70:358
116. Cuvelier D, Derenyi I, Bassereau P, Nassoy P (2005) Biophys J 88:2714
117. Sorre B, Callan-Jones A, Manzi J, Goud B, Prost J, Bassereau P, Roux A (2012) Proc Natl Acad Sci USA 109(1):173
118. Dimova R, Seifert U, Pouligny B, Förster S, Döbereiner HG (2002) Eur Phys J B 7:241
119. Heinrich V, Waugh RE (2006) Ann Biomed Eng 24:595
120. Hosu BG, Sun M, Marga F, Grandbois M, Forgacs G (2007) Phys Biol 4:67
121. Terasaki M, Chen LB, Fujiwara K (1986) J Cell Biol 103:1557
122. Vale RD, Hotani H (1988) J Cell Biol 107:2233
123. Roux A, Cappello G, Cartaud J, Prost J, Goud B, Bassereau P (2002) Proc Natl Acad Sci USA 100:15583
124. Koster G, Duijn MV, Hofs B, Dogterom M (2003) Proc Natl Acad Sci USA 100:15583

125. Karlsson A, Karlsson R, Karlsson M, Cans AS, Strömberg A, Ryttsén F, Orwar O (2001) Nature 409:150
126. Karlsson M, Sott K, Cans AS, Karlsson A, Karlsson R, Orwar O (2001) Langmuir 17:6754
127. Dasgupta R, Miettinen M, Lipowsky R, Dimova R (2018) Proc Nat Acad Sci USA 115:5756
128. Evans E, Needham D (1987) J Phys Chem 91:4219
129. Petros RA, DeSimone JM (2010) Nat Rev Drug Discov 9:615
130. Rodriguez PL, Harada T, Christian DA, Pantano DA, Tsai RK, Discher DE (2013) Science 339:971
131. Mahmoudi M, Meng J, Xue X, Liang XJ, Rahmand M, Pfeiffer C, Hartmann R, Gil PR, Pelaz B, Parak WJ, del Pino P, Carregal-Romero S, Kanaras AG, Selvan ST (2014) Biotechnol Adv 32:679
132. Agudo-Canalejo J, Lipowsky R (2015) Nano Lett 15:7168
133. Agudo-Canalejo J, Lipowsky R (2016) Soft Matter 12:8155
134. Agudo-Canalejo J, Lipowsky R (2017) Soft Matter 13:2155
135. Seifert U, Lipowsky R (1990) Phys Rev A 42:4768
136. Antonny B, Burd C, De Camilli P, Chen E, Daumke O, Faelber K, Ford M, Frolov VA, Frost A, Hinshaw JE, Kirchhausen T, Kozlov MM, Lenz M, Low HH, McMahon H, Merrifield C, Pollard TD, Robinson PJ, Roux A, Schmid S (2016) EMBO J 35:2270
137. Schöneberg J, Lee IH, Iwasa JH, Hurley JH (2017) Nat Rev Mol Cell Biol 18:5
138. Agudo-Canalejo J, Lipowsky R (2018) PLoS Comput Biol 14:e1006422
139. Sosale N, Rouhiparkouhi T, Bradshaw AM, Dimova R, Lipowsky R, Discher DE (2015) Blood 125:542
140. Bahrami AH, Lipowsky R, Weikl TR (2016) Soft Matter 12:581
141. Dasgupta S, Auth T, Gompper G (2014) Nano Lett 14:687
142. Bahrami AH, Lipowsky R, Weikl TR (2012) Phys Rev Lett 109:188102
143. Šarić A, Cacciuto A (2012) Phys Rev Lett 109:188101
144. Bahrami AH, Raatz M, Agudo-Canalejo J, Michel R, Curtis EM, Hall CK, Gradzielski M, Lipowsky R, Weikl TR (2014) Adv Colloid Interface Sci 208:214
145. Helfrich M, Mangeney-Slavin L, Long M, Djoko K, Keating C J Am Chem Soc 124:13374 (2002)
146. Albertsson PA (1986) Partition of cell particles and macromolecules: separation and purification of biomolecules, cell organelles membranes, and cells in aqueous polymer two-phase systems and their use in biochemical analysis and biotechnology, 3rd edn. Wiley, New York
147. Long MS, Cans AS, Keating CD (2008) J Am Chem Soc 130:756
148. Li Y, Lipowsky R Dimova R (2008) J Am Chem Soc 130:12252
149. Kusumaatmaja H, Li Y, Dimova R, Lipowsky R (2009) Phys Rev Lett 103:238103
150. Brangwynne CP, Eckmann CR, Courson DS, Rybarska A, Hoege C, Gharakhani J, Jülicher F, Hyman AA (2009) Science 324:1729
151. Knorr RL, Franzmann T, Feeney M, Frigerio L, Hyman A, Dimova R, Lipowsky R (manuscript in preparation)
152. Lipowsky R (2018) J Phys Chem B. 122:3572
153. Satarifard V, Grafmüller A, Lipowsky R ACS Nano (in press)
154. Knorr RL, Dimova R, Lipowsky R (2012) PLoS One 7:e32753
155. Knorr RL, Lipowsky R, Dimova R (2015) Autophagy 11:2134
156. Lipowsky R (2013) Faraday Discuss 161:571
157. Helfrich W, Harbich W (1987) Physics of amphiphilic layers. In: Meunier J, Langevin D, Boccara N (eds) Springer proceedings in physics, vol 21. Springer, Berlin, pp 58–63
158. Derzhanski A, Petrov AG, Mitov MD (1978) Ann Phys 3:297
159. Lorenzen S, Servuss RM, Helfrich W (1986) Biophys J 50:565
160. Marchi S, Patergnani S, Pinton P (2014) Biochim Biophys Acta 1837:461–469
161. van Weering JRT, Cullen PJ (2014) Semin Cell Dev Biol 31:40
162. Westrate LM, Lee JE, Prinz WA, Voeltz GK (2015) Annu Rev Biochem 84:791
163. Wang X, Gerdes HH (2015) Cell Death Differ 22:1181

164. He K, Luo W, Zhang Y, Liu F, Liu D, Xu L, Qin L, Xiong C, Lu Z Fang X, Zhang Y (2010) ACS Nano 6:3015
165. Sowinski S, Jolly C, Berninghausen O, Purbhoo MA, Chauveau A, Köhler K, Oddos S, Eissmann P, Brodsky FM, Hopkins C, Önfelt B, Sattenta Q, Davis DM (2008) Natl Cell Biol 10(2):211
166. Weiss M, Benk LT, Frohnmayer JP, Haller B, Janiesch JW, Heitkamp T, Börsch M, de Lira R, Dimova R, Lipowsky R, Bodenschatz E, Baret JC, Vidakovic-Koch T, Sundmacher K, Platzman I, Spatz JP (2018) Nat Mater 17:89